Climate change increased the likelihood of wildfire disaster in highly exposed Los Angeles area

Report finalised: January 28th 2025

Authors

Clair Barnes, *Centre for Environmental Policy, Imperial College, London, UK*
Theo Keeping, *Leverhulme Centre for Wildfires, Environment and Society, Imperial College London & School of Archaeology, Geography and Environmental Science, University of Reading*
Gavin Madakumbura, *Department of Geography, University of California, Los Angeles, California. USA*
John Abatzoglou, *Management of Complex Systems Department, University of California Merced, Merced, California, USA*
Park Williams, *Department of Geography, University of California, Los Angeles, California, USA*
Amir AghaKhouchak, *Department of Civil and Environmental Engineering, Department of Earth System Science, University of California, Irvine, USA*
Izidine Pinto, *Royal Netherlands Meteorological Institute (KNMI), De Bilt, The Netherlands*
Vikki Thompson, *Royal Netherlands Meteorological Institute (KNMI), De Bilt, The Netherlands*
Robert Vautard, *IPSL, CNRS, Paris, France*
Seppe Lampe, *Department of Water & Climate, Vrije Universiteit Brussel (VUB), Brussels, Belgium*
Wim Thiery, *Department of Water & Climate, Vrije Universiteit Brussel (VUB), Brussels, Belgium*
Rosa Pietroiusti, *Department of Water & Climate, Vrije Universiteit Brussel (VUB), Brussels, Belgium*
Friederike Otto, *Centre for Environmental Policy, Imperial College, London, UK*
Maja Vahlberg, *Red Cross Red Crescent Climate Centre, The Hague, The Netherlands; Swedish Red Cross, Stockholm, Sweden*
Roop Singh, *Red Cross Red Crescent Climate Centre, The Hague, The Netherlands*
Nicole Lambrou, *California State Polytechnic University, Pomona, USA*
Edward Blakely, *University of California, Berkeley, USA*
Yifang Zhu, *University of California, Los Angeles, USA*
Jing Li, *University of California, Los Angeles, USA*
Tarik Benmarhnia, *University of California, San Diego, USA*
Travis Longcore, *University of California, Los Angeles, USA*
Miriam Marlier, *University of California, Los Angeles, USA*
Emmanuel Raju, *Copenhagen Centre for Disaster Research, Global Health Section, Department of Public Health, University of Copenhagen, Copenhagen, Denmark*
Nick Baumgart, *Copenhagen Centre for Disaster Research, Global Health Section, Department of Public Health, University of Copenhagen, Copenhagen, Denmark*

Julie Arrighi, *Red Cross Red Crescent Climate Centre, The Hague, The Netherlands; American Red Cross, Washington D.C., USA; University of Twente, Enschede, The Netherlands*

Review authors

Niklas Merz, *Centre for Environmental Policy, Imperial College, London, UK*
Joyce Kimutai, *Centre for Environmental Policy, Imperial College, London, UK*
Sjoukje Philip, *Royal Netherlands Meteorological Institute (KNMI), De Bilt, The Netherlands*
Gerbrand Koren*, Copernicus Institute of Sustainable Development, Utrecht University, Utrecht, The Netherlands*
Sonny S. Patel, *Georgia State University, Atlanta, USA; Harvard University, Cambridge, USA*
Ann Bagala, *American Red Cross, Washington D.C., USA*
Lauren Rudd, *Red Cross Red Crescent Climate Centre, The Hague, The Netherlands*

Main Findings

- Coastal Southern California is an environment highly prone to catastrophic wildfires. The destructiveness of a fire thus also strongly depends not only on the weather conditions but also on whether land use and fire management strategies take these characteristics into account. The Palisades Fire occurred in an officially designated Very High Fire Hazard Severity Zone, while the Eaton Fire was only partly within such an area. This means fire risk has always been very high and building regulations require at least 200 ft of vegetation management around structures within the designated Very High Fire Hazard Severity Zones. Post-fire assessments will check compliance with these requirements.

- Looking at weather observations, in today's climate with 1.3°C global warming relative to preindustrial, the extreme Fire Weather Index (FWI) conditions that drove the LA fires are expected to occur on average once in 17 years. Compared to a 1.3°C cooler climate this is an increase in likelihood of about 35% and an increase in the intensity of the FWI of about 6%. This trend is however not linear, with high FWI conditions increasing faster in recent decades.

- To determine the role of climate change in this observed trend we combine the observation-based estimates with climate models. Eight of the eleven models examined also show an increase in extreme January FWI, increasing our confidence that climate change is driving this trend. Combining models and observations, we find that human-induced warming from burning fossil fuels made the peak January FWI more intense, with an estimated 6% increase in intensity, and 35% more probable. Fire weather indices consist of many variables, which are not always well represented by climate models. Wind, in particular, is often poorly represented. While we have high confidence in the qualitative change, that the likelihood and intensity of the FWI has increased due to human-induced climate change, the precise numbers have a wide range of uncertainty due to the model performance.

- This trend is projected to continue into the future, with peak FWI intensifying by a further 3% and similar values becoming a further 35% more likely if the world warms to 2.6°C, which is the lowest warming expected under current policies by 2100.

- We also assess the drought conditions leading up to the fires, using two different indices. First, we consider the October-December (OND) standardised precipitation index, which is defined relative to the 1991-2020 climatology and measures how dry OND 2024 was in comparison. We calculated the index for today's climate of 2024 and a 1.3° colder climate. Similarly dry seasons are expected to occur on average once every 20 years in the current climate; this is 2.4 times more likely than in a preindustrial climate. The OND ENSO conditions also increased the likelihood of the drought by a factor of 1.8 relative to neutral ENSO conditions. Climate models do not agree on the direction of precipitation trends in this region, so we are unable to formally attribute this change to global warming.

- We further assess changes in the timing of the end of the dry season. Analysing observations, we find that the length of the dry season has increased by about 23 days since the global climate was 1.3°C cooler. This means that, due to the burning of fossil fuels, the dry season, when a lot of fuel is available, and the Santa Ana winds, that are crucial for the initial spread of wildfires, are increasingly overlapping.

- Our observational analysis shows that the frequency of an atmospheric circulation pattern such as that of January 8th 2025, which is known to strengthen Santa Ana wind events, has increased in winter, raising the risk of weather conditions that drive the spread of wildfire.

Whether this trend is attributable to human-caused climate change requires a more in depth study of the patterns in observations and climate models.

- As an additional line of evidence, we analyse simulations from process-based fire models run under observed and counterfactual climate conditions, to estimate the expected effect of climate change on burned area in the region. These models suggest that the potential burned area in December-January in the Los Angeles area is today substantially higher than it would be in the absence of climate change. We note that these models represent changes in potential burned area driven by climate change but do not faithfully reproduce observed trends in burned area, and any real-world changes are the combined result of climate change and direct human interventions in the landscape.

- The Coastal Southern California region is a small area, often represented by only a few grid-boxes in climate models and gridded observational products. Furthermore, the complexity of the weather conditions characterising fire weather and large year to year variability in rainfall means that precise numbers in every single line of evidence are uncertain. However, the lines of evidence examined overall point in the same direction, indicating that conditions that make extreme fires more likely are increasing. This is also in line with existing literature, as summarised by the IPCC (AR6 WGI, Chapter 12), that shows an increase in high temperatures, combined with a drying in the larger area and thus higher fire risk. Given all these lines of evidence we have high confidence that human-induced climate change, primarily driven by the burning of fossil fuels, increased the likelihood of the devastating LA fires.

- The elderly, people living with disability (especially limited mobility), lower-income people without personal vehicles, and population groups that received late warnings were disproportionately impacted, as they had a more difficult time getting to safety. The neighborhood of Altadena with a large Black population was in the path of the fires, which destroyed the major source of generational wealth for many residents who had previously faced discriminatory redlining practices.

- The wildfires exposed critical weaknesses in the city's water infrastructure, designed for routine fires rather than the extreme demands of large-scale fires. The crisis highlighted the need for strategic investments in resilient water systems and improved pressure management, alongside stronger climate adaptation and emergency preparedness measures to address more frequent future wildfires.

1 Introduction

Starting on January 7 2025 two large wildfires (the Palisades and Eaton Fires) erupted in Los Angeles County, California. Over the following weeks more than 50,000 acres burned, fuelled by exceptionally wildfire-prone conditions. These wildfires had devastating effects due to very strong Santa Ana winds, low fuel moisture and fuel continuity conditions, all of which are highly conducive to a very rapid fire spread, making the wildfires extremely difficult to contain. It is the most destructive wildfire event to have affected Los Angeles in its history, with 16,252 structures recorded as destroyed by the California Department of Forestry and Fire Protection (CAL FIRE) at the time of writing. The Palisades and Eaton wildfires are the second and third most destructive wildfires in California, trailing only the Camp Fire of 2018 by number of structures destroyed.

The Southern California Geographic Area Coordination Centre (GACC) experienced an average of 380,000 acres of burned area from 2013 to 2023, with Coastal Southern California having a Mediterranean climate primarily vegetated by fire-adapted chaparral and oak. Coastal Southern California is bordered to the north and east by a strip of mountains, known as the Southern California mountains, with the coastline running from northwest to southwest.

Southern California's fire regime is unique, as large fires can occur nearly year round. In summer, generally July through September, large fires are often promoted by extremely low fuel moistures arising because summer precipitation is rare and evaporative demand is high due to a combination of high temperatures, low humidity, and intense solar radiation. These summer fires typically occur in the foothills and mountains of southern California, often in the absence of significant wind events and often are topographically driven moving uphill and away from where most of the 25 million residents in southern California reside. Beginning around October, evaporative demand is generally lower but very fast moving and destructive fires can nonetheless occur if a strong wind event occurs prior to the onset of the cool-season rains, which usually begin from October-November. These winds are known as Santa Ana winds and they are most common in wintertime, but their ability to drive fire in mid-winter is usually nullified because winter is the peak of California's rainy season. When the onset of the rainy season is delayed and/or the Santa Ana windy season arrives early, wildfire danger can be extreme, as vegetation generally has not seen meaningful amounts of precipitation since the prior spring and is critically dry (Cayan et al., 2022). The coincidence of dry fuels and winds can pose further potential for large, fast-moving fires when fuels are abnormally abundant due to anomalously wet conditions over the preceding one or two years (Khorshidi et al., 2020). Importantly, wildfire is a natural part of the Californian ecosystem and many vegetation species are highly adapted to, and in some cases dependent on, fire. On the other hand, the vast majority of wildfires in Coastal Southern California are ignited by humans or human infrastructure, and humans are responsible for essentially all wind-driven fires that ignite in fall and winter (Kolden & Abatzoglou, 2018).

The 2025 Los Angeles Fires were exceptional in terms of the speed at which the wildfires developed, the difficulty of suppressing such fast-spreading wildfires in high wind conditions, and the significant population immediately downwind of ignitions. The Santa Ana winds are most frequent after the end of the dry season, when higher fuel moisture suppresses wildfire likelihood, but have contributed to large cool-season wildfire events in the past when they precede the onset of the winter rainy season (Miller & Schlegel, 2006; Cayan et al. 2022). The summer of 2024 was one of the warmest on record in Southern California, during which three notable large fires (Line, Bridge and Airport Fires) occurred. These fires burned over 120,000 acres and damaged or destroyed nearly 300 structures. As the cool, wet season approached, the typical onset of the rainy season did not arrive. However, the Santa Ana winds arrived, coinciding with very dry fuels. Furthermore, wildland and wildland-urban interface (WUI) vegetation continuity was higher than average, as the region received anomalously high precipitation starting from the 2023 rainy season, which typically begins around October, and extending into the spring of 2024. In addition to anomalously high precipitation totals in the cool seasons of 2022/23 and 2023/24, the summer of 2023 was also very wet due to Hurricane Hilary, a once-in-a-lifetime event that brought high rainfall totals to much of Southern California in August. Wildfires in this Mediterranean climate region are often fuel-limited, meaning they are positively correlated with antecedent wet conditions, which act as a good proxy for fuel growth (Williams et al., 2019).

A primary way in which climate change affects wildfire is through a strong, warming-driven increase of the atmosphere's vapour pressure deficit, which exerts a drying effect on vegetation ([Abatzoglou and Williams, 2016](); [Williams et al., 2019]()). As the atmosphere warms, its moisture capacity increases, resulting in an increasing likelihood of greater extremes in its evaporative demand. Additionally, the same greater moisture capacity drives higher evaporation rates from the ocean, so when precipitation events do occur, there may be more atmospheric moisture available to fuel high-intensity precipitation ([O'Gorman et al., 2009]()). This means that the likelihood of a wet, highly conducive year to moisture-responsive plant growth (as is common in Coastal Southern California) being followed by a dry, highly conducive year to wildfire is likely increasing with climate change due to so-called hydroclimate whiplash ([Swain et al., 2025]()). Further, climate models project reduced precipitation totals and frequencies in the fall in southern California, constituting a delay in the rainy season that would, all else equal, increasingly leave dry fuels exposed to the onset of the Santa Ana windy season ([Goss et al., 2020]()). On the other hand, it is expected that global warming may promote a slight reduction in the frequency of early season (mainly Sep-Nov) Santa Ana winds due to a decreasing cool-season temperature differential between the ocean and continental interior, but this has not yet been observed and little change in the magnitude of the strongest events is anticipated ([Guzman-Morales and Gershunov, 2019]()). Additionally, atmospheric humidity associated with Santa Ana wind events in a warming climate is projected to become even lower, increasing their vegetation desiccating potential ([Hughes et al. 2011](), [Gershunov et al. 2021]()).

Although the damages caused by these wildfires have yet to be completely assessed, it is clear that they have resulted in human health impacts including 28 deaths, along with widespread property, and commercial losses. The reconstruction of large areas of burned residences and infrastructure will result in significant costs; private insured losses are estimated to be [27.2 billion USD](), whilst AccuWeather estimated that total losses were greater than [250 billion USD]().

1.1 Wildfires in Southern California

The wind-driven fires of Southern California, similar to the destructive Palisade and Eaton fires investigated in this report, occur during windy and dry offshore Santa Ana wind events. The intensity of some past fires can be directly linked to factors such as a delay in the rainy season, anomalous warmth during the summer and fall, an abundance of fuel from current and previous wet years, and dead vegetation left behind by multi-year droughts ([Westerling et al., 2004]()).

One notable wildfire season that experienced all these factors was 2003. The four-year period leading up to the fires experienced abnormally dry conditions, followed by extreme heat with temperatures exceeding 100°F (37.8°C) and very low humidity, leaving an abundance of dry fuel for fires ([NWS]()). During the late October to early November period, wildfires killed 22 people, destroyed 3,600 homes, and burned nearly 740,000 acres ([NWS]()).

Two other notable Santa Ana wind driven fires caused immense destruction in Southern California during the last decade, following the multiyear drought of 2012–2016 in California. The first is the Thomas Fire of 2017, which occurred during the longest-duration Santa Ana wind event in 70 years ([Kolden & Abatzoglou, 2018]()) and the driest March-to-December period at the time ([LA Times]()). The fire spread across Santa Barbara and Ventura counties, burning 281,893 acres, damaging 274 structures, and destroying 1,063 structures ([CAL FIRE]()). The second is the Woolsey Fire of 2018,

which started in Ventura County and spread to Los Angeles County. This fire burned 96,949 acres, damaged 364 structures, destroyed 1,643 structures, and caused three fatalities (CAL FIRE).

In an assessment of the emergence of changes in FWI across the world, Abatzoglou et al., (2019) find that enhanced fire weather conditions emerge in the first half of the 21st century in most burnable regions across the world, while in Southern California there is evidence of an anthropogenic increase in some fire weather metrics in the early to mid 21st century. Abatzoglou and Williams (2016) find that from 1984 to 2015, over 4 million ha, or approximately half of burned forest area in the western US was attributable to climate change. However, in southern California, and particularly in the non-forested regions such as those that burned in January 2025, wildfire activity is dictated by far more than fire weather and there has been no observed trend in cool-season area burned since at least the early 1970s (Williams et al., 2019).

The IPCC assessment indicates that fire weather conditions, which promote the likelihood of wildfires, have been shown to become more prevalent in Mexico and throughout Western and North-Western North America, largely due to rising temperatures. As climate change continues, these conditions are expected to worsen, particularly in the southwestern regions of North America, with a high degree of confidence. By 2050, a significant increase in the Fire Weather Index (FWI) is projected, alongside a longer fire weather season and higher peak FWI values, signaling more frequent and intense fire risks in the near future (Ranasinghe et al, 2021).

In a review of extreme weather events from an attribution perspective, Clarke et al., (2022) identified Western North America, the wider region including Southern California, as one of two regions in the world where there is very high confidence in future increase in wildfire risk and an attributable signal has already emerged.

1.2 Event Definitions

Because of the highly complex nature of fire weather in this region, we carry out trend attribution for several indices to capture different relevant aspects of the antecedent conditions, as defined below.

The study region is the Southern California Level III Ecoregion of North America (Omernik and Griffith, 2014), referred to throughout this report as the Coastal Southern California region (outlined in red in Figure 1.1a). Due to the relatively small extent of this region, time series were generated from gridded data by first weighting each grid-cell according to the proportion of the cell intersecting with the ecoregion, and then averaging over all intersecting grid cells.

1.2.1 Peak January FWI

To capture the short-term intensity of the fire weather conditions associated with the fires, we use the 1-day January maximum of the fire weather index (FWI) averaged over the study region. The FWI is a composite fire-risk index that accounts for longer-term drying conditions as well as wind and humidity driven conditions that can drive wildfire spread on a given day. Figure 1.1a shows a map of the FWI on January 8th 2025, the day on which the fires broke out and the day on which the peak

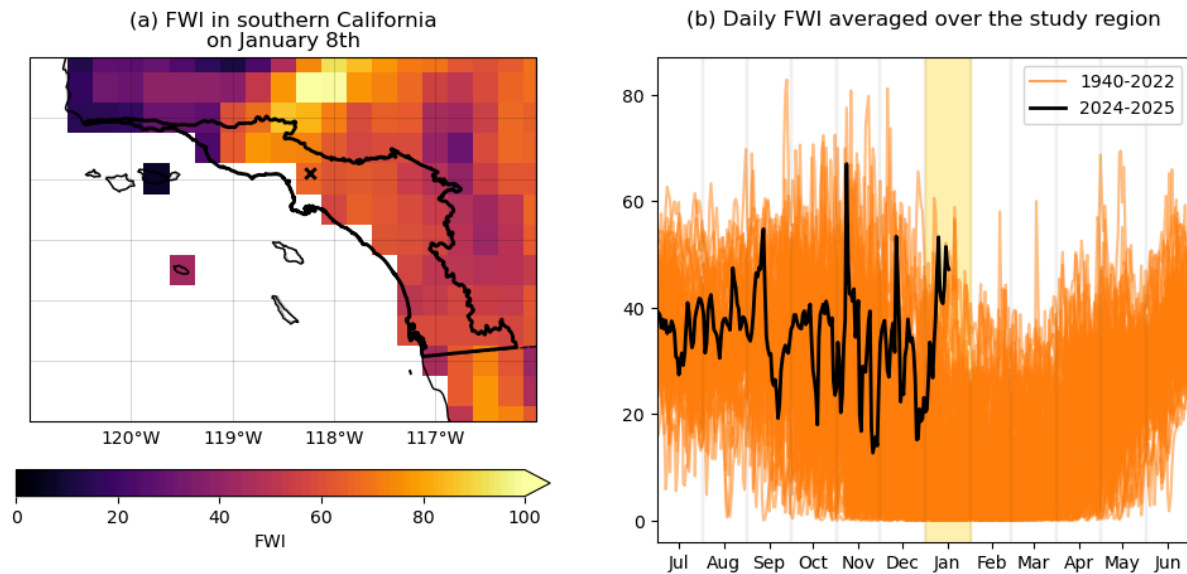January FWI occurred (Figure 1.1b).At the time of writing, ERA5 reanalysis data were available up to January 15th.

Figure 1.1 *(a) Map of FWI based on ERA5 data on 8th of January 2025, showing very high indices around LA (black cross). The red polygon denotes the study area and corresponds to Coastal Southern California. (b) Daily FWI based on ERA5 in 2024/2025 (black) compared to recent years since 1991 (orange). January is highlighted in yellow.*

1.2.2 October-December SPI

The last three months of 2024 were exceptionally dry (Figure 1.2), and followed two relatively wet winters (panel b). To examine trends in the dry conditions in the three months leading up to the fires, we analyse the October-December (OND) mean precipitation averaged over the study region outlined in red in Figure 1.1a. To obtain a better-fitting statistical model, we calculate the Standardised Precipitation Index (SPI). We do this by first fitting a gamma distribution to the OND mean precipitation values from 1991-2020, to obtain estimates of the parameters of the climatological distribution. These parameters are used to find the cumulative distribution function of each year's OND precipitation, which is the probability that the rainfall would be less than or equal to that value. These probabilities are then mapped onto a standard Gaussian distribution, so that each value is expressed in standard deviations from the climatological mean. To test the sensitivity to the period used in the standardisation, the analysis was repeated with SPI standardised with respect to the full available dataset (1940-2024), with qualitatively similar results.
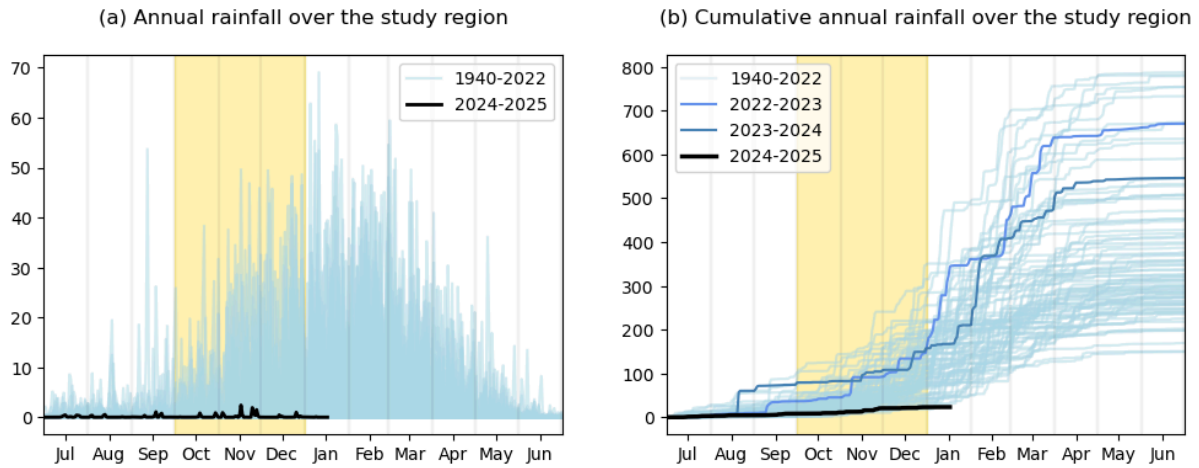
Figure 1.2: *(a) Annual rainfall and (b) cumulative annual rainfall over the study region (mm), compared to recent years (ERA5). October-December are highlighted in yellow.*

1.2.3 Timing of the end of drought conditions

A key factor in the 2025 fires has been the overlap of the dry season with the Santa Ana wind season. To examine the question of whether this overlap is increasing due to climate change, we use the drought code (a sub-index of the FWI, as described in Section 2.4) to characterise drought conditions (Fig. 1.3), and define the drought end date as the day of the hydrological year (starting on September 1st) on which the greatest absolute 7-day drop in the drought code occurs. This approach is preferred to more standard rainy-season metrics because the drought code accounts for evapotranspiration as well as precipitation, giving a more realistic picture of the drought conditions; and because the formulation is not sensitive to user-specified thresholds in precipitation quantity, which can pick up heavy rainfall events that are nonetheless not drought-ending, due to subsequent periods of drying .
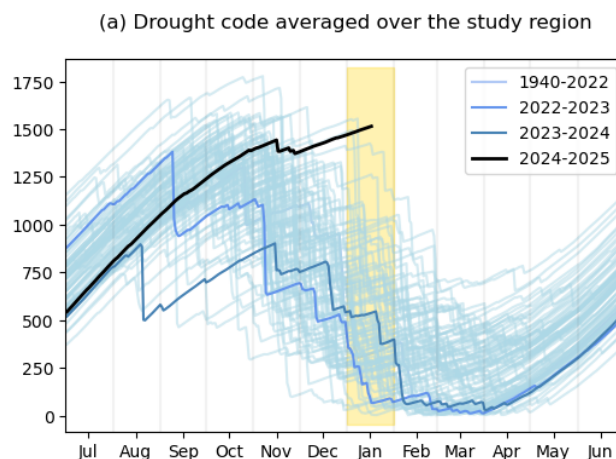

Figure 1.3: *Drought Code of the FWI over the study region in 2024/25, compared to recent years (ERA5). January is highlighted in yellow.*

Data and methods used in probabilistic attribution

In this report, we study the influence of anthropogenic climate change by comparing the likelihood and intensity of similar fire weather extremes in the 2025 climate with those in a 1.3 °C cooler climate. We also extend this analysis into the future by assessing the influence of a further 1.3 °C of global warming from present. This is in line with the latest Emissions Gap Report from the United Nations Environment Programme, which shows that the world is on track for at least 2.6 °C temperature rise given currently implemented policies (UNEP, 2024). We also consider the effect of the current ENSO state on the fire weather conditions.

2.1 Observational data

The European Centre for Medium-Range Weather Forecasts's 5th generation reanalysis product, ERA5, is a gridded dataset that combines historical observations into global estimates using advanced modelling and data assimilation systems (Hersbach et al., 2020). For the analysis of the FWI, we use temperature, relative humidity and wind speed at 10 m recorded at noon, as well as 24-h precipitation. For analysis of the October-December drought conditions we also use the precipitation, and the drought code uses both temperature and precipitation. All data from this product is at a resolution of 0.25°×0.25°, from the years 1950 to present.

To characterise the large-scale drivers affecting these extremes indices, we use the following datasets as covariates:
- As a measure of anthropogenic climate change we use the (low-pass filtered) global mean surface temperature (GMST), where GMST is taken from the National Aeronautics and Space Administration (NASA) Goddard Institute for Space Science (GISS) surface temperature analysis (GISTEMP, Hansen et al., 2010 and Lenssen et al. 2019). GMST is expressed in the figures as an anomaly with respect to 2025, in °C.
- As a measure of the El Niño - Southern Oscillation cycle (ENSO) we use the detrended Niño3.4 index during October-December (OND). This is computed from NOAA's ERSST v.5 sea surface temperatures, by subtracting the mean tropical SST (20S-20N) from the mean SST over the Nino3.4 region (5S-5N, 170W-120W). This index is therefore adjusted to remove the trend associated with climate change as proposed in van Oldenborgh et al., 2021, but without rescaling each calendar month.

2.2 Model and experiment descriptions

We use 2 multi-model ensembles from climate modelling experiments using very different framings (Philip et al., 2020): Sea Surface temperature (SST) driven global circulation high resolution models and regional climate models.

1. Coordinated Regional Climate Downscaling Experiment (CORDEX) - The North America (CORDEX-NAM) data archive contains output from regional climate models (RCMs) run over a domain covering most of North America using boundary conditions from global climate model (GCM) simulations in the CMIP5 archive. These simulations run from 1950–2100 with a spatial

resolution of 0.22°/25km or 0.44°/50km (Mearns et al., 2017), composed of historical simulations up to 2005, and extended to the year 2100 using the RCP8.5 scenario.

2. HighResMIP SST-forced model ensemble (Haarsma et al. 2016), the simulations for which span from 1950 to 2050. The SST and sea ice forcings for the period 1950-2014 are obtained from the 0.25° x 0.25° Hadley Centre Global Sea Ice and Sea Surface Temperature dataset that have undergone area-weighted regridding to match the climate model resolution. For the 'future' time period (2015-2050), SST/sea-ice data are derived from RCP8.5 (CMIP5) data, and combined with greenhouse gas forcings from SSP5-8.5 (CMIP6) simulations (see Section 3.3 of Haarsma et al. 2016 for further details).

2.3 Statistical methods

Methods for observational and model analysis and for model evaluation and synthesis are used according to the World Weather Attribution Protocol, described in Philip et al., (2020), with supporting details found in van Oldenborgh et al., (2021), Ciavarella et al., (2021) and here. The key steps, presented in sections 3-6, are: (3) trend estimation from observations; (4) model validation; (5) multi-method multi-model attribution; and (6) synthesis of the attribution statement. Table 2.1 summarises the time series and the statistical distributions and assumptions used to model the changes due to each covariate.

Time series	Distribution	Nonstationarity assumption
FWI (1-day January maximum)	GEV	Shift
SPI (October-December)	Gaussian	Shift
Drought Code	Gaussian	Shift

Table 2.1: *Summary of time series of indices and statistical models used to estimate the influence of different covariates in these metrics.*

For each time series we calculate the return period and intensity of the event under study for the 2024 GMST and for 1.3°C cooler GMST: this allows us to compare the climate of now and of the preindustrial past (1850-1900, based on the Global Warming Index), by calculating the probability ratio (PR; the factor-change in the event's probability) and change in intensity of the event.

2.3.1 Statistical modelling of trends

The El-Niño Southern Oscillation (ENSO) is known to affect fire weather and drought conditions in this region at certain times of the year (section 1.2). Therefore, we first investigate the effect of including this as an additional covariate in the statistical model (section 2.3). ENSO is represented by the relative Niño3.4 index, averaged over the October-December (OND) period. The typical peak of the oscillation occurs in December-February, so in this case OND is as close as possible to the peak given the timing of this event. Fitting a statistical model using both GMST and this ENSO index as covariates gives an improved fit than GMST alone, according to the Akaike Information Criterion, a

standard model selection criterion. The influence of the current (OND) ENSO state is therefore considered in the observational analysis in Section 3. The covariate is included in the attribution modelling, but only results for changes associated with GMST changes are reported.

In order to examine the effect of the ENSO phase on each index alongside that of increasing GMST, we extend the nonstationary model to accommodate an additional covariate. All results quoted are from a statistical model including both covariates. For instance, the variable of interest, FWI, is assumed to follow a GEV distribution in which the location parameter varies with both GMST and ENSO:

$$X \sim GEV(\mu, \sigma, \xi \mid \mu_0, \sigma_0, \alpha, \beta, T, I),$$

where X denotes the variable of interest, FWI; T is the smoothed GMST; I is the detrended Niño3.4 index; μ_0, σ_0 and ξ are the location, scale and shape parameters of the nonstationary distribution; and α, β are the trends due to GMST and ENSO, respectively. As a result, the location of the distribution has a different value in each year, determined by both the GMST and Niño3.4 states. Maximum likelihood estimation is used to estimate the model parameters, with

$$\mu = \mu_0 + \alpha T + \beta I \qquad \text{and} \qquad \sigma = \sigma_0.$$

Under this model, the effects of GMST and the detrended Niño3.4 index are assumed to be independent of one another, so that the change in intensity due to GMST is unaffected by the change in intensity due to the ENSO phase. We note that this may not be the case in the real world, as the intensity and frequency of El Niño events may have been influenced by climate change (Cai et al., 2021); however, by using a detrended Niño3.4 index (see Section 2.1) we aim to minimise the correlation between the two factors, and so do not expect the qualitative findings of this study to be affected by this simplifying assumption.

2.3.2 Defining the ENSO state in climate models

The multi-method multi-model attribution step of the WWA protocol involves estimating, for each climate model, the effective return level of a 1-in-n-year event under the current climate state, and estimating the expected change in likelihood and intensity of such an event after a specified change in the covariates. Because the smoothed GMST is generally monotonically increasing, the standard WWA approach is simply to take the model's 2025 GMST as a covariate and to estimate the expected magnitude of an n-year event. However, the factual climate in this study is defined by the 2025 GMST and by the mean of the detrended Niño3.4 index during the rainy season. During the attribution step, the detrended Niño3.4 index derived from the climate model is standardised so that the subset from 1940-2024 has mean 0 and variance 1; the 'factual' climate is then defined as having the model's 2025 GMST and the 2024 observed value of the detrended Niño3.4 index, standardised in the same way. This removes any potential biases in the results due to differences between the amplitude of the modelled Niño3.4 index and that observed.

2.3.3 Synthesis of results from observations and climate models

Synthesis plots present the estimated changes in intensity or likelihood of the event of interest from both observational datasets (shown as blue bars) and climate models (red bars), along with weighted and unweighted averages of this information that is used to give an overarching attribution statement. The best estimate for each dataset is marked with a black triangle, while the coloured bars represent a 95% confidence interval obtained by bootstrapping. When more than one observational data product is used, a term to account for the spread of the best estimates is added in quadrature to the natural variability of each dataset: this is shown in the figures as a white box around the light blue bars. The dark blue bar indicates the average of the observational data products, including this additional uncertainty. Similarly, a term to account for intermodel spread is added in quadrature to the natural variability of the models: this is shown in the figures as white boxes around the light red bars. The dark red bar shows the weighted model average, where the weights are derived from the precision (inverse of the variance) of each model estimate.

Observation-based products and models are combined into a single result in two ways - a detailed description including the mathematical formulations can be found in the literature (Philip et al., 2020; Li & Otto, 2022; Otto et al., 2024). Firstly, we neglect common model uncertainties beyond the intermodel spread already incorporated in the observational and model averages, and compute the precision-weighted average of models (dark red bar) and observations (dark blue bar): this weighted mean is indicated by the magenta bar. To account for the fact that, due to common model biases, model uncertainty can be larger than the intermodel spread, we also show an unweighted average of the synthesised observations (dark blue bar) and models (dark red bar), indicated by the black outline in the bottom row of the synthesis figures.

2.4 Calculation of the Fire Weather Index

The FWI consists of three initial sub-indices that are calculated using temperature, relative humidity and wind speed at 10m recorded at noon, as well as 24-h precipitation. These subindices are the fine fuel moisture code (FFMC), the duff moisture code (DMC), and the drought code (DC), with values from the previous day feeding back into the system to model changes in fuel moisture on different time scales (days, weeks and months, respectively). As shown in Figure 2.1, these three subindices are combined via the initial spread index (ISI) and the buildup index (BUI) to generate the final FWI value. The FWI and its subindices were computed using the xclim package (Bourgault et al., 2023). For ERA5, the FWI and subindices were calculated using the noon temperature, relative humidity and surface windspeed, and antecedent precipitation in the prior 24 hours. Climate model data was downloaded directly from the GridMET bias-corrected NAM-22 CORDEX FWI dataset (NCAR, 2024).
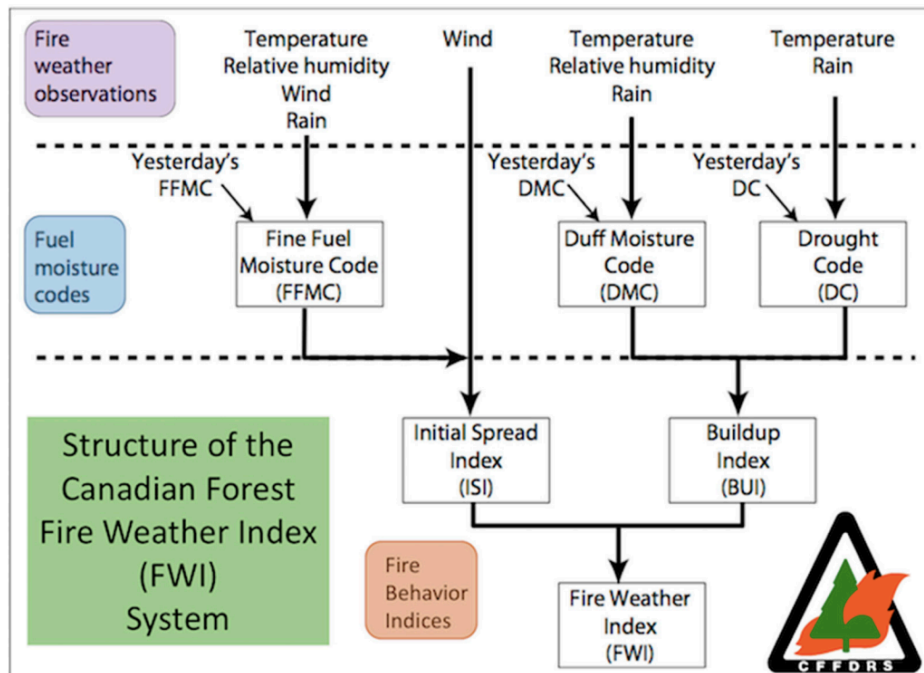
Figure 2.1: Structure of the Canadian Forest Fire Weather Index (*Van Wagner, (1974)*; image courtesy of *UQAM*)

3 Trend attribution

3.1 Peak January FWI

Peak daily January FWI (hereafter FWI1X) averaged over the Coastal Southern Californian ecoregion is modelled using a GEV in which the location parameter is assumed to depend linearly on the covariates, while the scale and shape parameters are fixed.

3.1.1 Observed trends

Figure 3.1 shows FWI1X in the ERA5 dataset, as a function of time and of the two covariates (GMST and Niño3.4 OND). The nonparametric smoothed trend (dashed green line) is not linear in GMST, due to a period of persistently low values from 1980-2000; however, it does show that FWI1X was consistently lower at the beginning of the time series than in the present climate, so we are confident that the fitted trend (black line) is picking up the correct signal of an increase in FWI1X, although it may be under-estimating the strength of the underlying linear trend, which has been much stronger since 1980; it is not clear whether this is an artefact of the data prior to the satellite era or a real effect, perhaps due to changing aerosol concentrations. The quality in the first 10 to 20 years of ERA5 might also be lower, however excluding them does not materially affect the quality of the fit, so we use the whole dataset. The smoothed trend in FWI1X as a function of OND Niño3.4 is fairly linear, indicating that the linear model is able to represent the relationship, with lower FWI1X expected under El Niño conditions and higher during La Niña-like conditions.
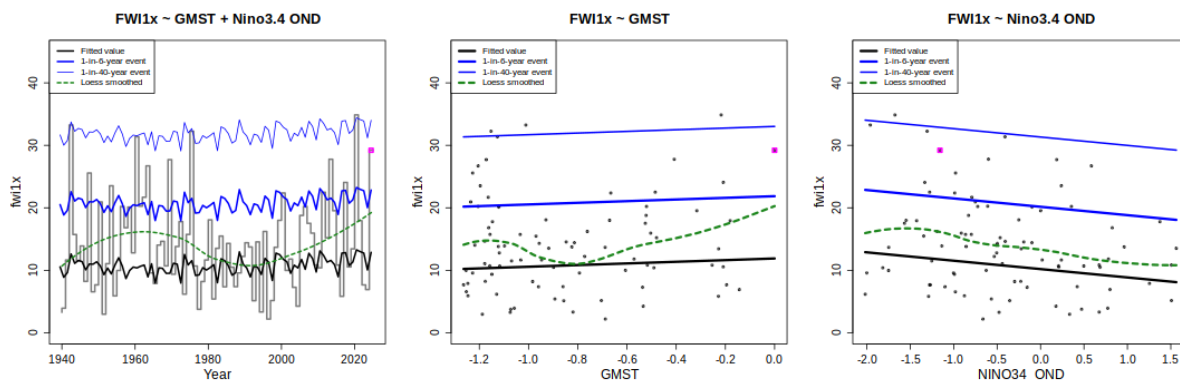

Figure 3.1: ERA5 FWI1x and fitted linear trends. The heavy black line indicates the location of the distribution; blue lines indicate the 6-year and 40-year expected return level; the green dashed line is a nonparametric Loess smoother and the pink dot shows FWI1X in January 2025. (a) Fitted trend over time; (b) FWI1X as a function of GMST anomaly from 2025, in °C, with Niño3.4 covariate fixed at its mean level; (c) FWI1X as a function of OND Niño3.4 index, with GMST fixed at its mean level.

Return level plots, showing the change in expected return levels of events of increasing rarity, are shown in Figure 3.2. The model fits the data reasonably well, with all points lying within the shaded region indicating 95% confidence bounds. The factual and counterfactual scenarios are only slightly separated, reflecting the relatively weak trend in FWI1X.
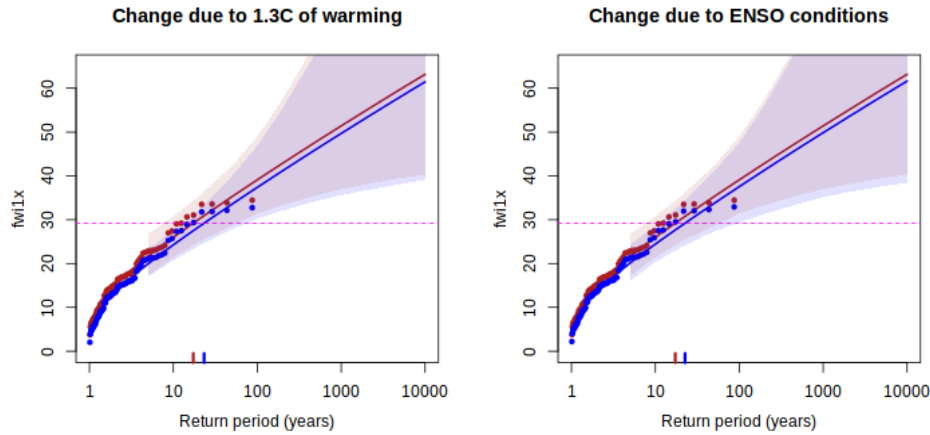
Figure 3.2: *Expected return levels in FWI1X over the study region in the 2025 climate (red lines) and in a counterfactual climate (blue line), estimated from the statistical model. Shaded regions represent 95% confidence intervals obtained via a bootstrapping procedure. The pink line shows the peak FWI during January 2025. Red and blue ticks at the x axis indicate the estimated return level of January 8th in the 2025 climate and counterfactual climate. (a) Counterfactual climate is 1.3°C cooler than 2025, but has 2024's October-December mean ENSO state; (b) counterfactual climate has 2025 GMST and neutral ENSO state (OND Niño3.4 is fixed at zero).*

The observed maximum daily FWI between January 1st and 15th 2025 (the available data at the time of writing) occurred on January 8th. The estimated return period and changes in intensity and likelihood of this event are summarised in Table 3.1. The FWI value on January 8 2025 was unusual but not unprecedented, with an estimated return period of 17 years in the current climate and under current ENSO conditions. According to the model, both global warming and the preceding ENSO state have increased the intensity of January FWI1X by 5-6%, and increased the likelihood of observing similarly extreme FWI1X values by 30-35%, although the uncertainty about the contribution from global warming is somewhat higher. The trends in GMST and ENSO are statistically independent (having a Pearson correlation coefficient of -0.06) and these effects are therefore compounding: similarly extreme FWI1X values are now 75% more likely to occur than they would have been in in a neutral ENSO phase and in a preindustrial climate, and around 12% more intense.

Dataset	Return period	Probability ratio		Change in FWI1X		% Change in FWI1X	
		GMST	ENSO	GMST	ENSO	GMST	ENSO
ERA5	17 (8 - 56)	1.35 (0.44 - 4.8)	1.31 (1.0 - 2.1)	1.7 (-3.5 - 7.5)	1.6 (0.3 - 3.4)	6.2% (-10.8 - 35)	5.6% (1.1 - 13)

Table 3.1: *Summary of fitted model results for FWI1X. Return period of 2025 FWI1X maximum in the 2025 climate; probability ratio, absolute change in FWI1X and % change in FWI1X associated with 1.3°C of global warming (GMST) and with OND 2024 La Niña conditions (detrended Niño index of -1.16), when compared to neutral conditions. Light orange indicates a best-estimate increase in FWI1X, while dark orange indicates a statistically significant increase in FWI1X.*

3.1.2 Multi-method multi-model attribution

We now combine the observational results from Section 3.2.1 with results from the same statistical analysis applied to climate model data. Due to the small study area and requirement that models provide wind speeds and relative humidity as well as precipitation and temperatures, only relatively high-resolution regional climate models have been used in this analysis. Of eleven CORDEX models with the required variables, only six passed the model evaluation step and are included in the final attribution synthesis, the results of which are summarised in Table 3.2. For details of how the results are synthesised and how to interpret the synthesis plots, see Section 2.3.3. See Table A1.1 for details of the model evaluation and Table A2.1 for the full attribution results.

Figure 3.3 shows the changes in probability and relative intensity of a 1-in-20-year event associated with an increase of 1.3°C in GMST. As already noted in Section 3.1.1, in the ERA5 reanalysis product FWI1X increases with GMST, although the trend is not strictly linear and the uncertainty surrounding the best estimate is high. Two of the six climate models that passed model evaluation exhibit no GMST-dependent trend in FWI1x, but the remaining four simulate an increase of comparable or larger magnitude than the observed increase. Overall, the synthesised result is of an increase of 5.7% in peak January FWI intensity (95% interval: -10.4% - +27.4%) and a probability ratio of 1.37 (0.48 - 3.6): a 37% increase in the likelihood of experiencing similarly extreme January FWI in 2025 compared to in a preindustrial climate. The high uncertainty surrounding these numbers is expected: we are evaluating changes in the most extreme value of FWI in a single month (January) of each year, in a region where climatic variability is known to be particularly high (Dettinger et al., 2011), and using only a small number of observational datasets and climate models. However, the congruence between the trends in ERA5 and the climate models gives us greater confidence that this is a climate change signal. Furthermore, the trend is projected to continue as the world continues to warm (Figure 3.4), with a further 3% increase in intensity and a further increase of 37% in the likelihood of experiencing similarly extreme one-day January FWI after 1.3° more warming.
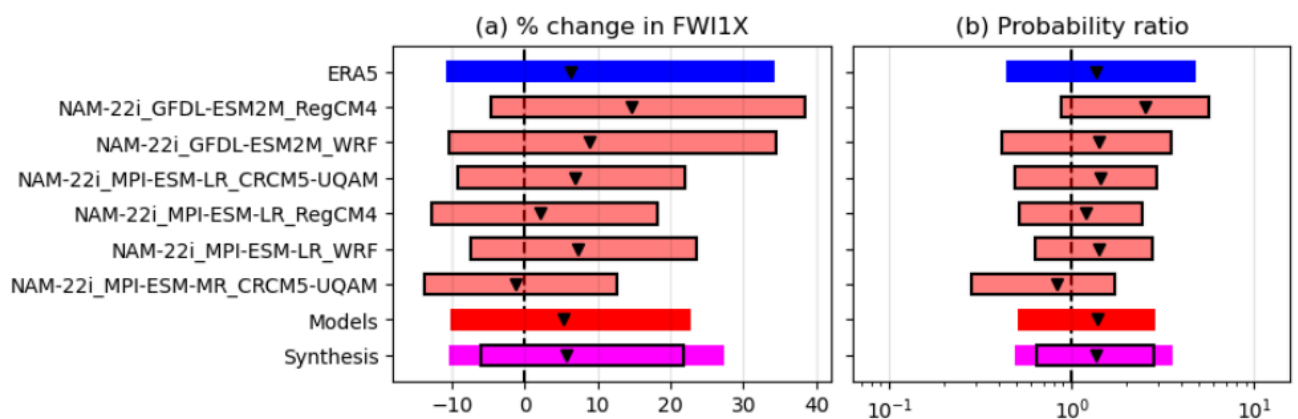

Figure 3.3: *Synthesis of (left) relative intensity changes and (right) probability ratios when comparing the return period and magnitudes of January FWI1X in Coastal Southern California between the current climate and a 1.3°C cooler climate. See Section 2.3.3 for further details.*
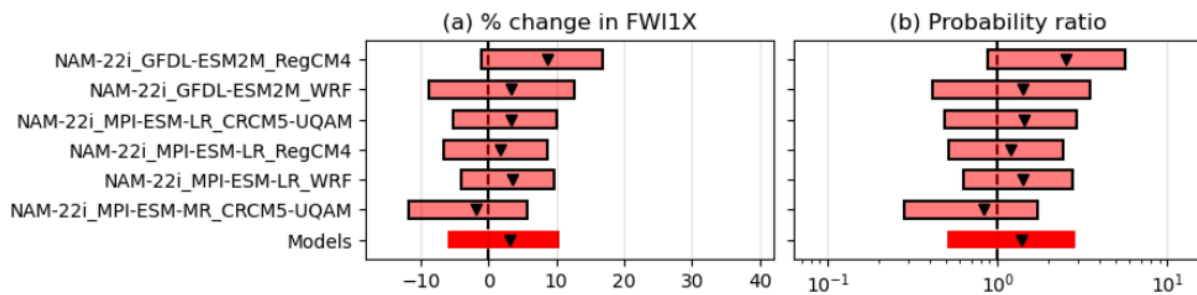
Figure 3.4: *As Figure 3.3, synthesising changes in January FWI1X between the current climate and a climate with a further 1.3°C of warming (that is, a climate that is 2.6C warmer than preindustrial).*

Data		% intensity change (95% CI)	Probability ratio (95% CI)
Observations	**Past- Present**	6.26 (-10.8 - 34.4)	1.34 (0.44 - 4.8)
Models		5.33 (-10.2 - 22.7)	1.37 (0.51 - 2.9)
Synthesis		5.67 (-10.4 - 27.4)	1.37 (0.48 - 3.6)
Models only	**Present- Future**	3.22 (-5.9 - 10.5)	1.37 (0.51 - 2.9)

Table 3.2: *Synthesised reanalysis and model results for changes in FWI1X associated with increasing GMST, as presented in Figures 3.3 and 3.4. Statistically significant increases (decreases) in probability and intensity are highlighted in dark blue (orange), while non-significant increases are highlighted in light blue (orange).*

3.2 October-December SPI

The SPI is calculated by fitting a gamma distribution to the OND precipitation values during the climatological calibration period (1991-2020), and using the fitted parameters to calculate the cumulative distribution function of each year's precipitation. These are then mapped onto the corresponding percentiles of a standard normal distribution, to which the nonstationary statistical model is fitted: this formulation is more tractable than attempting to fit a nonstationary gamma distribution directly to the OND precipitation. By mapping the gamma distribution onto a standard normal distribution, the SPI expresses precipitation in terms of standard deviations above or below the average, while taking into account the skewed distribution of the raw rainfall data.

October-December SPI (hereafter SPI-OND) is modelled using a Gaussian distribution in which the mean is assumed to depend linearly on the covariates, while the standard deviation remains fixed. An alternative model was also tested, in which both the mean and standard deviation can vary with the covariates; while, by eye, this appeared to better capture the variability associated with the ENSO

covariate, model selection criteria (AIC) indicated that the fit was not sufficiently improved to justify the extra parameter. We therefore report results for the simpler model here, noting that the estimated mean trends were similar in both models; only the estimated return periods and probability ratios changed, and the uncertainty around all estimates was much higher.

3.2.1 Observed trends

Figure 3.5 shows the October-December SPI in the ERA5 dataset, as a function of time and of the two covariates. In all three panels, the fitted model trend (black line) corresponds fairly well to the nonparametric smoothed trend (dashed green line), indicating that the model does a good job of capturing the main trends in the data, with SPI decreasing as the climate warms, and lower SPI during La Niña conditions than El Niño conditions, although the trend is rather weak. This weak trend is reflected by the small separation between the two distributions in the return level plots (Figure 3.6). All points lie close to the estimated return level, indicating that the model fits the data well.
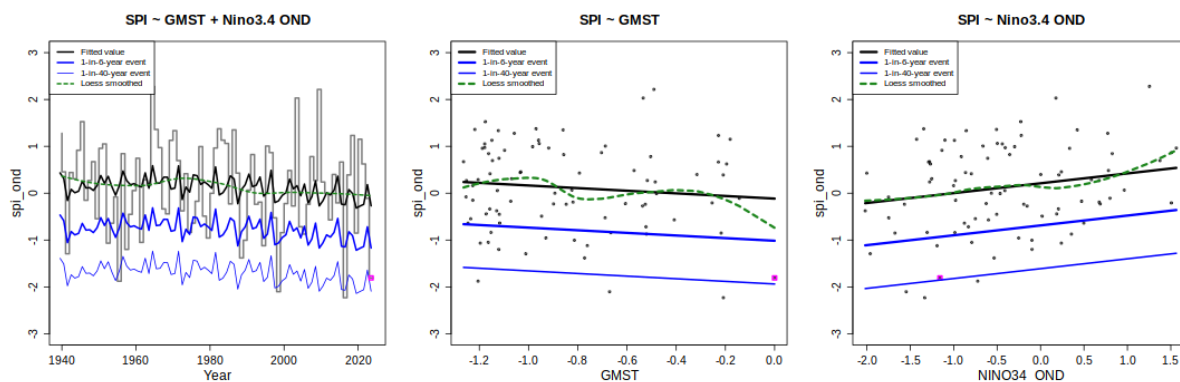

Figure 3.5: *ERA5 SPI-OND and fitted linear trends. The heavy black line indicates the location of the distribution; blue lines indicate the 6-year and 40-year expected return level; the green dashed line is a nonparametric Loess smoother and the pink dot shows the SPI in October-December 2024. (a) Fitted trend over time; (b) SPI-OND as a function of GMST anomaly from 2025, in °C, with Niño3.4 covariate fixed at its mean level; (c) SPI-OND as a function of OND Niño3.4 index, with GMST fixed at its mean level.*
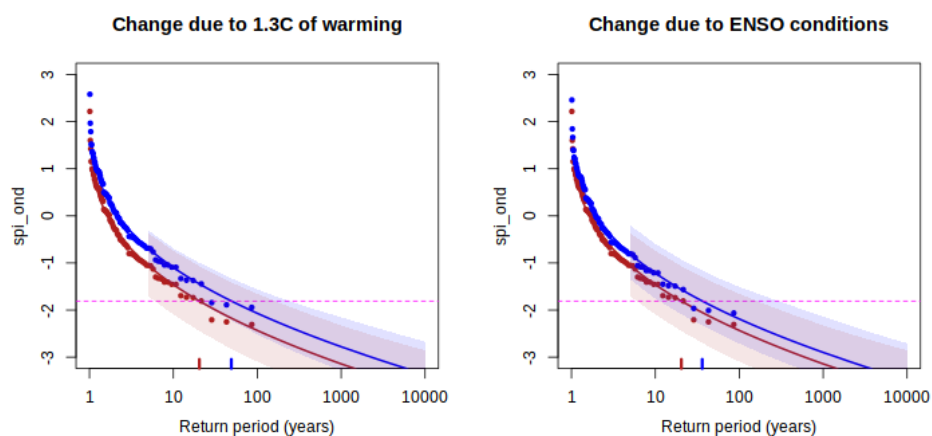

Figure 3.6: *Expected return levels of SPI-OND over the study region in the 2025 climate (red lines) and in a counterfactual climate (blue lines), estimated from the statistical model. Shaded regions represent 95%*

confidence intervals obtained via a bootstrapping procedure. The pink line shows the observed SPI-ONDin 2024. Red and blue ticks at the x axis indicate the estimated return level of January 8th in the 2025 climate and counterfactual climate. (a) Counterfactual climate is 1.3°C cooler than 2025, but has 2024's October-December mean ENSO state; (b) counterfactual climate has 2025 GMST and neutral ENSO state (OND Niño3.4 is fixed at zero).

The SPI during October-December 2024 was -1.81, a value characterised by NASA as 'severely dry' (NASA, 2025). The estimated return period and changes in intensity and likelihood of this event are summarised in Table 3.3. An October-December SPI as low as observed in 2024 is unusual but not unprecedented, with an estimated return period of 20 years in the current climate and under current ENSO conditions. Both global warming and the preceding ENSO state are associated with lower SPI and increased likelihood of similarly dry seasons, although neither signal is statistically significant: similarly low SPI-OND is 2.4 times more likely in the current climate than if the climate were 1.3°C cooler, and 1.8 times more likely under La Nina- conditions than in a neutral ENSO phase. The effect of these two factors together means that similarly low SPI-OND values are an estimated 4.7 times more likely to occur in the current climate than they would have been in a neutral ENSO phase in a preindustrial climate.

Dataset	Return period	Probability ratio		Change in SPI-OND	
		GMST	ENSO	GMST	ENSO
ERA5	20 (6 - 161)	2.4 (0.33 - 20.9)	1.8 (0.95 - 3.2)	-0.36 (-1.2 - 0.4)	-0.24 (-0.4 - 0.02)

Table 3.3: *Summary of fitted model results for SPI-OND in the ERA5 dataset. Return period of 2024 SPI-OND maximum in the 2025 climate; probability ratio, change in SPI-OND and equivalent change in precipitation associated with 1.3°C of global warming (GMST) and with OND 2024 La Niña conditions (detrended Niño index of -1.16), when compared to neutral conditions. Light orange indicates a decrease in SPI-OND, while dark orange indicates a statistically significant decrease in SPI-OND.*

3.2.2 Multi-method multi-model attribution

We now combine the observational results from Section 3.2.1 with results from the same statistical analysis applied to climate model data. We again use an ensemble of regional climate models in the attribution step, but this time supplemented with HighResMIP climate models (see Section 2.2), for which daily precipitation data is available. Of twelve CORDEX models evaluated, nine were judged 'good' in the model evaluation step and are included in the final attribution synthesis. Of eight variants of the IPSL-CM6A and IPSL-CM7A model, five were judged 'good' and included in the synthesis as a single ensemble of models, although these runs do not include simulations beyond 2014 and so are not included in the synthesis of projected changes. Of twelve SST-forced HighResMIP models, two were found to perform poorly; of the remaining ten, four were excluded as duplicates of higher-resolution models, leaving six independent models. The results of the attribution synthesis are summarised in Table 3.4. For details of how the results are synthesised and how to interpret the plots,

see Section 2.3.3. See Table A1.2 for details of the model evaluation and Table A2.2 for the full attribution results.

Figure 3.7 shows the synthesised changes in SPI and probability of what is today a 1-in-20-year event, which is associated with an increase of 1.3°C in GMST from a preindustrial climate. As already noted, the ERA5 reanalysis shows a decrease in SPI-OND associated with increased GMST, albeit with high uncertainty. The CORDEX models (with names beginning 'NAM-' in the figures and tables) show no agreement on the direction of trends in SPI; however, five of the six HighResMIP models also simulate a reduction in SPI-OND of similar magnitude to the ERA5 trend. Overall, the synthesised response to a 1.3°C increase in GMST (bright pink bars) is a reduction of 0.23 standard deviations compared to a preindustrial climate (95% confidence interval: -0.93 to 0.46), and a probability ratio of 1.61 (0.31 - 11.6): an estimated 61% increase in the likelihood of experiencing a similarly dry October-December period in 2024 compared to in a preindustrial climate, suggesting that without anthropogenic warming, similarly October-December dry periods would have occurred only once every 49 years. Notably, the extreme nature of the negative SPI-OND anomaly in 2024 makes uncertainty ranges regarding the true return interval and the influence of anthropogenic climate change inherently wide and the estimated 61% increase in likelihood due to climate change is statistically insignificant. Under a further 1.3°C of warming from the present climate, the models collectively project very little change in SPI-OND (Figure 3.8). However, we note that had we considered only the HighResMIP models - which were produced as part of CMIP6 activity, and so are based on a later generation of models than the CORDEX simulations - the overall synthesised trends would be similar to the trend observed in ERA5 (Table 3.4b). This suggests that the observed drying trend in OND is attributable to climate change, although the signal is not reproduced by the earlier generation of climate models.
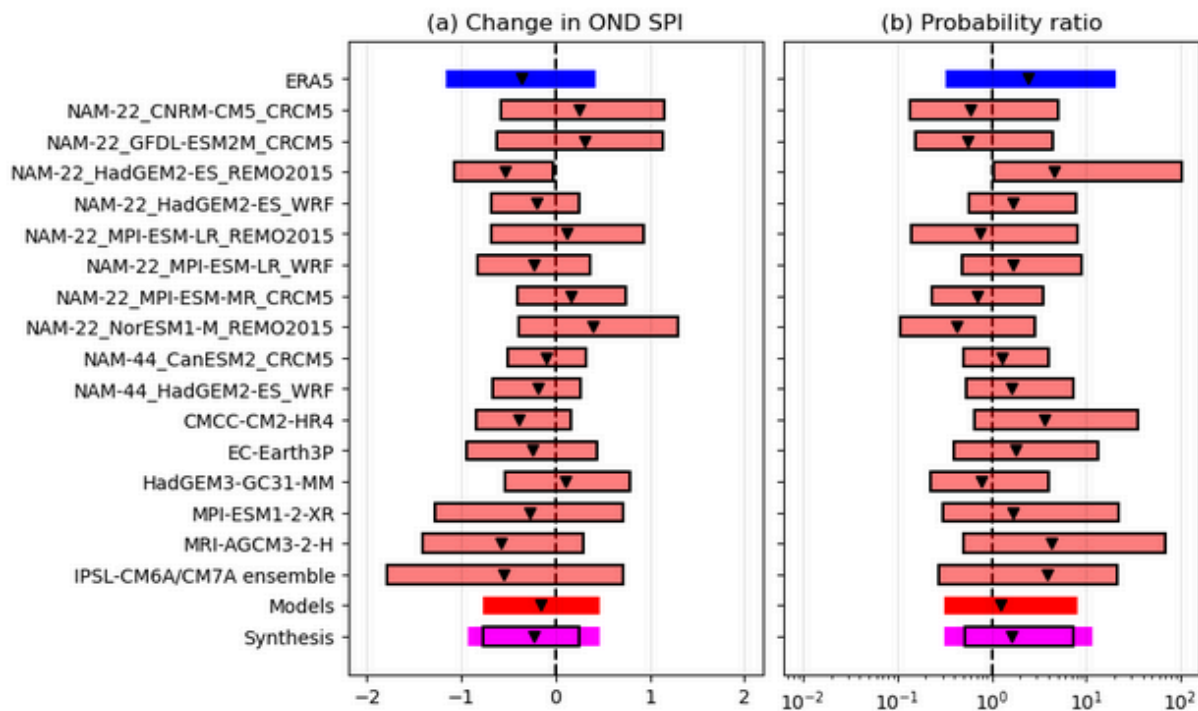

Figure 3.7: *Synthesis of (left) relative intensity changes and (right) probability ratios when comparing the return period and magnitudes of SPI-OND in Coastal Southern California between the current climate and a 1.3°C cooler climate. See Section 2.3.3 for further details.*
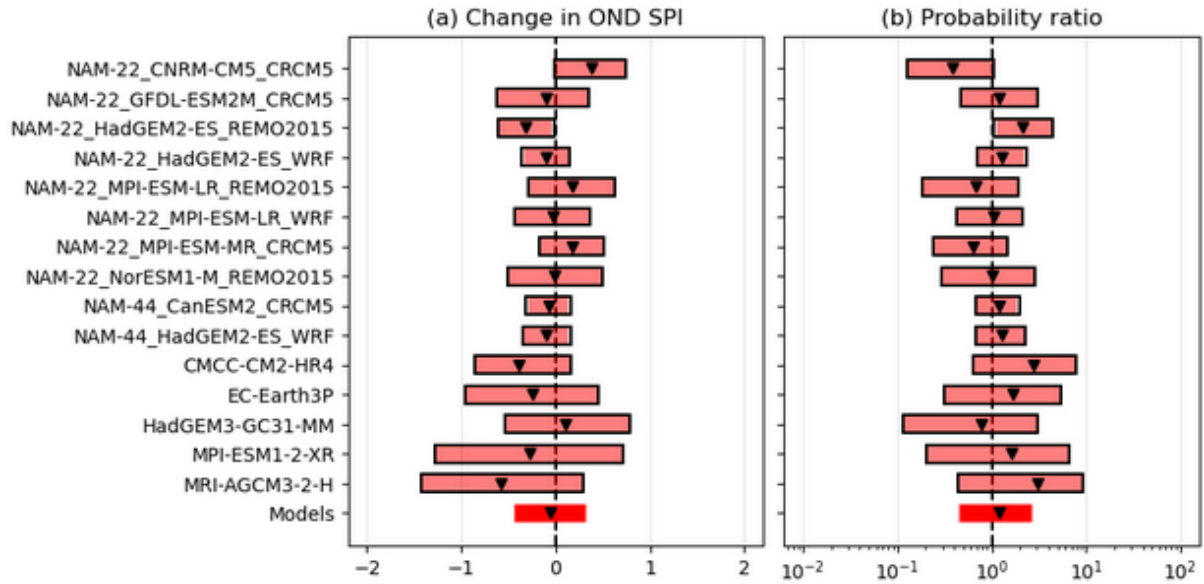
Figure 3.8: *As Figure 3.7, synthesising changes in SPI-OND between the current climate and a 1.3°C warmer climate (that is, a climate that is 2.6C warmer than preindustrial).*

		(a) All models		(b) HighResMIP only	
Data		**Change in SPI (95% CI)**	**Probability ratio (95% CI)**	**Change in SPI (95% CI)**	**Probability ratio (95% CI)**
ERA5	**Past-Present**	-0.36 (-1.2 - 0.4)	2.41 (0.33 - 20.9)	-0.36 (-1.2 - 0.4)	2.41 (0.33 - 20.9)
Models		-0.16 (-0.77 - 0.47)	1.26 (0.32 - 8.03)	-0.29 (-0.99 - 0.46)	1.88 (0.32 - 15.3)
Synthesis		-0.23 (-0.93 - 0.46)	1.61 (0.31 - 11.58)	-0.32 (1.07 - 0.44)	2.10 (0.32 - 17.6)
Models only	**Present-Future**	-0.06 (-0.44 - 0.31)	1.19 (0.45 - 2.65)	-0.27 (-0.93 - 0.43)	1.90 (0.33 - 6.17)

Table 3.4: *Synthesised reanalysis and model results for changes in SPI-OND associated with increasing GMST, as presented in Figures 3.7 and 3.8. Statistically significant decreases in SPI / increases in likelihood are highlighted in dark orange, non-significant decreases in SPI / increases in likelihood are highlighted in light orange. (a) Synthesis of reanalysis with all climate models that passed evaluation; (b) synthesis of reanalysis with only HighResMIP models.*

3.3 Timing of the end of the dry season

The day of the year on which the largest 7-day drop in the drought code occurs (hereafter, DC-DOY) is modelled using a Gaussian distribution, in which the mean is assumed to depend linearly on the GMST and ENSO covariates, while the standard deviation remains fixed. While the day of the year is recorded as an integer value, it can take a wide range of value and its distribution is approximately symmetrical, so the normal distribution is assumed to be appropriate.

3.3.1 Observed trends

Figure 3.5 shows the day of the hydrological year (starting on September 1st) on which the largest 7-day drop in DC occurs in the ERA5 dataset, as a function of time and of the two covariates. Again, the fitted model trend (black line) corresponds fairly well to the nonparametric smoothed trend (dashed green line), indicating that the trends are fairly linear and are therefore well represented by the linear model. The end of the season tends to be later in a warmer climate or in La Niña years. This weak trend is reflected by the small separation between the two distributions in the return level plots (Figure 3.6). All points lie close to the estimated return level, indicating that the model fits the data well.
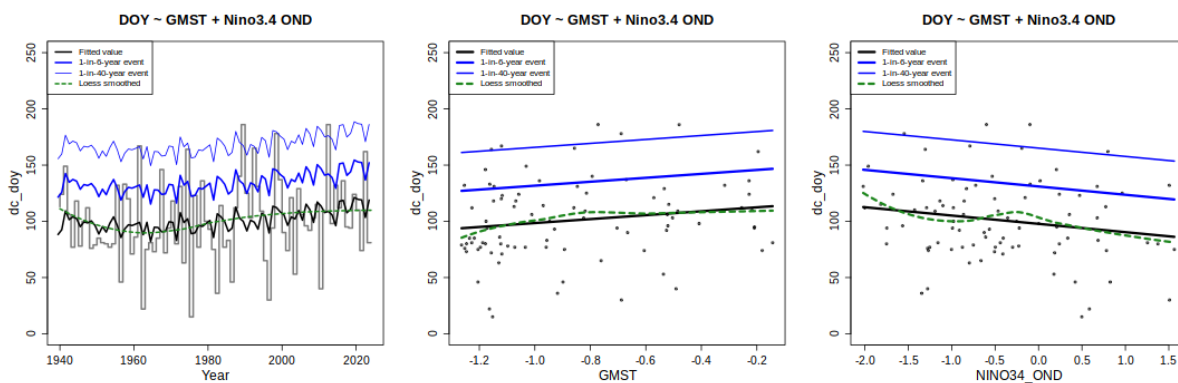

Figure 3.9: *Day of hydrologic year (days since 1 September) on which the drought season ends (DC-DOY) in ERA5, with fitted linear trends. The heavy black line indicates the location of the distribution; blue lines indicate the 6-year and 40-year expected return level; the green dashed line is a nonparametric Loess smoother. At the time of writing the 2024-25 dry season was still ongoing, so there is no observed value. (a) Fitted trend over time; (b) DC-DOY as a function of GMST anomaly from 2025, in °C, with Niño3.4 covariate fixed at its mean level; (c) DC-DOY as a function of OND Niño3.4 index, with GMST fixed at its mean level.*
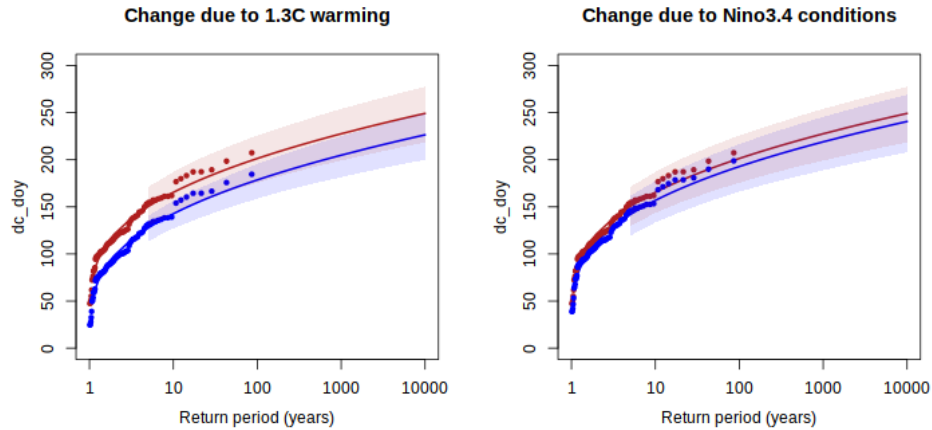
Figure 3.10: *Expected return levels of DC-DOY over the study region in the 2025 climate (red lines) and in a counterfactual climate (blue line), estimated from the statistical model. Shaded regions represent 95% confidence intervals obtained via a bootstrapping procedure. Red and blue ticks at the x axis indicate the estimated return level of January 8th in the 2025 climate and counterfactual climate. (a) Counterfactual climate is 1.3°C cooler than 2025, but has 2024's October-December mean ENSO state; (b) counterfactual climate has 2025 GMST and neutral ENSO state (OND Niño3.4 is fixed at zero).*

At the time of writing, the 2024-25 dry season has not yet ended, so we have no observed value from which to estimate the return period and hence the probability ratios, therefore we only report the change in timing of the end of the dry season. The estimated changes in the timing of the end of the dry season are summarised in Table 3.5. Both global warming and the preceding ENSO state are associated with a later end to the dry season; although the bootstrapped confidence intervals encompass the possibility of no change, both are heavily skewed toward a later end, with GMST showing a somewhat stronger signal.

Dataset	Change in day of year	
	GMST	**ENSO**
ERA5	23 (-2.7 - 49)	8.6 (-1.3 - 18)

Table 3.5: *Summary of fitted model results for DC-DOY. Absolute change in DC-DOY associated with 1.3°C of global warming and with OND 2024 La Niña conditions (detrended Niño index of -1.16), when compared to neutral conditions. Light orange indicates a delay in the timing of the end of drought conditions, while dark orange indicates a statistically significant delay in the end of drought conditions.*

3.3.2 Multi-method multi-model attribution

We now combine the observational results from Section 3.3.1 with results from the same statistical analysis applied to climate model data. We again use an ensemble of regional climate models in the attribution step supplemented with HighResMIP climate models (see Section 2.2), for which daily precipitation data and daily maximum temperatures are available. Of eight CORDEX models evaluated, five were judged 'good' in the model evaluation step and two reasonable; due to the very

small number of models available, all of these models are included in the final attribution synthesis. Of seven SST-forced HighResMIP model runs, one was found to perform poorly; of the remaining six, two were excluded as duplicates of higher-resolution models, leaving four independent models. The results of the attribution synthesis are summarised in Table 3.6. For details of how the results are synthesised and how to interpret the plots, see Section 2.3.3. See Table A1.3 for details of the model evaluation and Table A2.3 for the full attribution results.

Data		Change in day of year (95% CI)	Probability ratio (95% CI)
Observations	Past- Present	22.7 (-2.7 - 49.1)	1.29 (0.97 - 1.8)
Models		-0.86 (-25.3 - 24.1)	1.14 (0.27 - 4.0)
Synthesis		10.4 (-14.6 - 36.1)	1.28 (0.84 - 1.97)
Models only	Present- Future	0.23 (-18.4 - 18.7)	1.14 (0.27 - 4.0)

Table 3.6: *Synthesised reanalysis and model results for changes in the day of year on which the drought season ends, as presented in Figures 3.11 and 3.12. Statistically significant delays in the end of the season / increases in likelihood are highlighted in dark orange, non-significant decreases in SPI / increases in likelihood are highlighted in light orange. Rows corresponding to a change of less than 1 day are not shaded.*

Figure 3.11 shows the synthesised changes in the end of the drought season and changes in the probability of what is now a 1-in-10-year event, associated with an increase of 1.3°C in GMST from a preindustrial climate. As discussed previously, ERA5 records a delay of 23 days in the end of the drought season, which while not statistically significant at the 5% level would be significant at the 10% level. All of the CORDEX models that passed model evaluation exhibit a somewhat earlier end of the drought season; however, two of the four HighResMIP models also simulate significant delays in the season end and a third simulates a slight delay. Collectively, the climate models exhibit no clear signal, and so we cannot confidently attribute the observed change to anthropogenic warming, nor do we attempt to project future changes in the timing. However, the timing of the drought end index is sensitive to how droughts and wetting periods are defined, and will also be sensitive to how well the climate models capture the seasonal cycle and temporal granularity of rainfall events, so the high uncertainty about these estimates and lack of agreement among the climate models are not surprising. Previous research has detected a delay of a similar length in the onset of the rainy season and found this shift to be consistent with projections of future climate across California (Goss et al., 2020; Lukovic et al., 2021; Swain, 2021; Dong et al., 2022) so we conclude it is likely that the observed trend toward a delayed end of the drought season was promoted by anthropogenic warming, but that due to the small size of the region evaluated in this study, we do not detect a consistent signal in the climate models in our analysis.
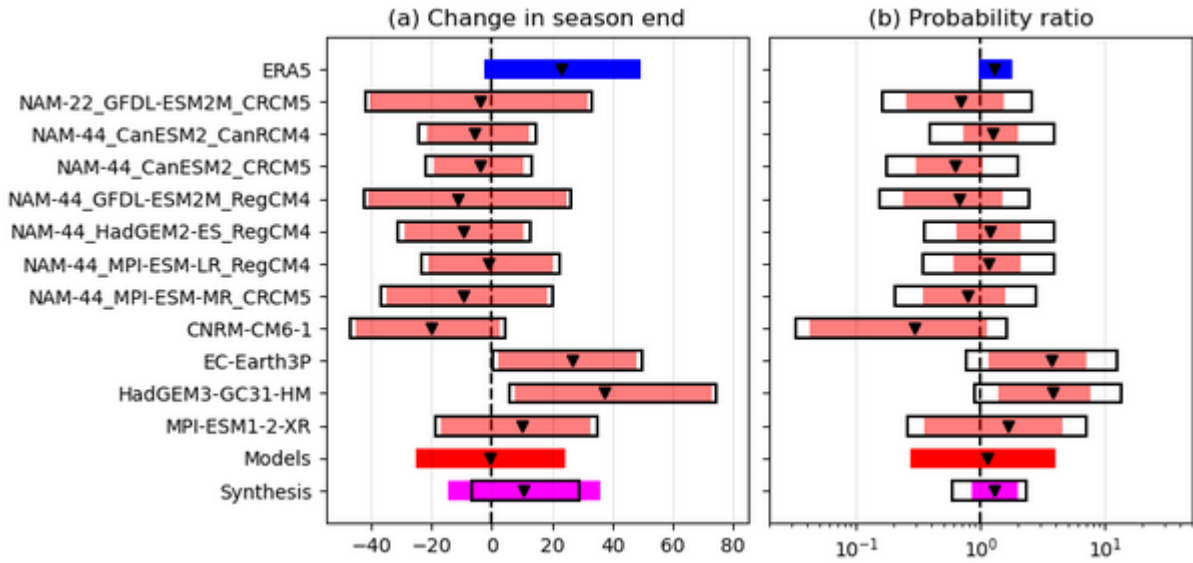
Figure 3.11: *Synthesis of (left) relative intensity changes and (right) probability ratios when comparing the return period and magnitudes of DC-DOY in Coastal Southern California between the current climate and a 1.3°C cooler climate. See Section 2.3.3 for further details.*
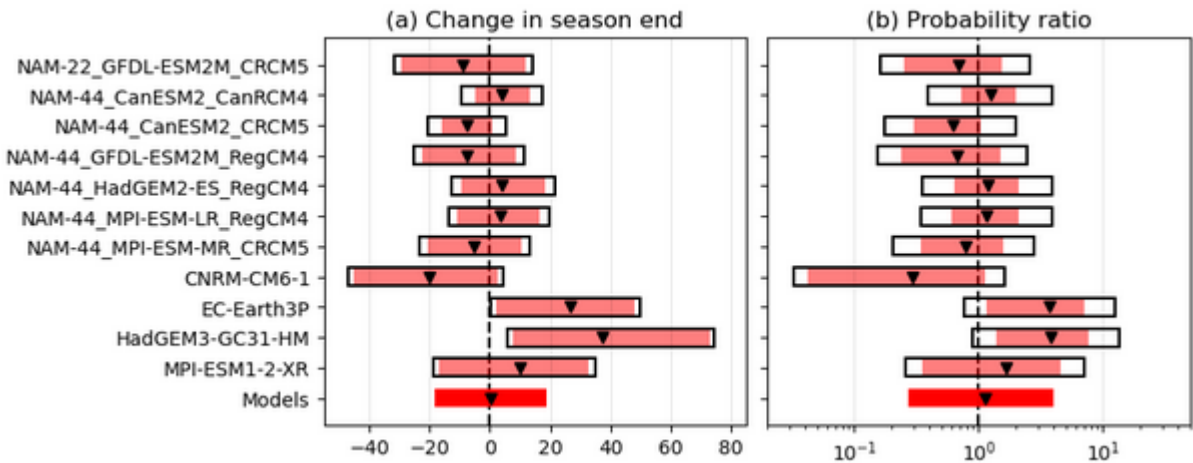

Figure 3.12: *As Figure 3.11, synthesising changes in DC-DOY between the current climate and a 1.3°C warmer climate (that is, a climate that is 2.6C warmer than preindustrial).*

4 Trends in Circulation

4.1 Data and methods

Atmospheric flow analogues can be used to assess changes in dynamically similar events or changes in the frequency of circulations (Cattiaux et al., 2010; Vautard et al., 2016; Jézéquel et al., 2018, Thompson et al 2024). Here we use ERA5 data to assess analogues identified from 500 hPa geopotential height (Z500) since 1950, to detect trends in the frequency of analogue circulations of those that occurred during the fire event.

To identify the most similar events, we compute the Euclidean distance between the Z500 field of the event day and every other day within DJF (1950–2023) over the region bounded by [-130° to -100°E, 20° to 45°N]. To avoid double-counting persistent events, the identified events must be separated by at least 5 days.

We identify the closest 27 events across two periods: an early period (1950-1979), defined by weaker climate change signal and a later period (1994-2023), characterised by a stronger climate change signal. This corresponds to the closest 1% of days in each period. The two sets of analogues are then compared to assess changes through time. This approach has the advantage of having two alternative sets of events, one fully adjusted to climate change. However, differences in modes of internal variability between the two time periods can impact the conclusions - we therefore cannot determine the role of climate change by comparing analogue sets alone in reanalyses. We also assess the change in frequency of the closest analogues through time. This is assessed at three different thresholds - the upper 5% of days, upper 10%, and upper 20%. The analogues within the upper 20% will not be as similar to the event itself, but will show some of the dynamical characteristics.

Furthermore, we explored the changes through time of an index that characterizes the specific circulation that induced strong North-Easterly winds in the Los Angeles area. We build a simplified index (IC) to characterize cut-off lows (COLs) similar to that of January 8th 2025, which can create a substantial effect on winds in Los Angeles. The index is defined as the 500 hPa geopotential difference between two locations, the first is the center of the cut-off low shown in Figure 4.1 (P1: 113.875°W; 30.875°N, where the geopotential is minimal), and the second point is located at P2: 122.875°W; 37.875°N). This difference, when largely negative as on the 8 January (-282 m) is in most cases corresponding to a cut-off low of the same kind, and also induces a pressure gradient associated with strong mid-troposphere North-Easterly winds. We have analyzed this index for the December to February months to increase statistics, but results are qualitatively similar when using only January.
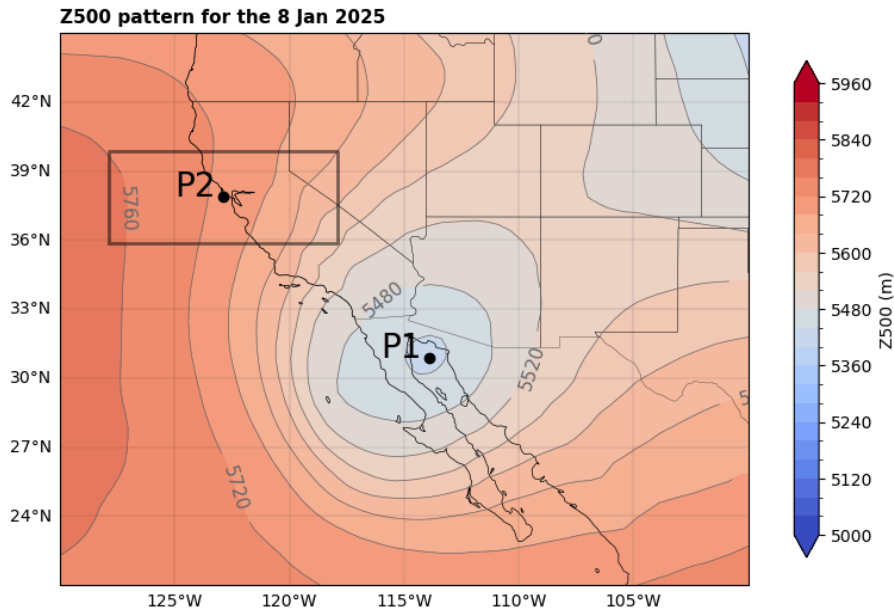
Figure 4.1 *500hPa geopotential height field for the event on the 8 Jan 2025. The box around P2 represents the area where alternative locations of P2 were considered in a sensitivity analysis Data ERA5*

4.2 Results

Southern California wildfires are commonly driven by strong offshore and dry Santa Ana winds (SAW), which typically occur between October and April (Jin et al 2015). Analysis of data from 1948 to 2018 by Keeley et al (2021) found that the most significant fires coincided with SAW events, with December and January identified as particularly critical months for SAW activity, though October has historically been the dominant month for SAW-associated fires. SAW events arise when high pressure develops over the Great Basin to the east, while a low-pressure system forms in the coastal area. Such atmospheric conditions were observed on January 8, 2025, for which a cut-off-low developed, as depicted by the 500 hPa geopotential height (Figures 4.1 and 4.2 a), strengthening the North-Easterly flow near the surface. We show how events similar to the atmospheric upper-level flow of 8 January 2025 have changed in the present (1994–2023) compared to the past (1950–1979). There is a significant deepening of the cut-off low over southern California, with the analogues in the present period 40m deeper than the past period (Figure 4.2d). A deeper cut-off low would lead to stronger winds in the region impacted by wildfire. Similar trends in analogues were also identified by ClimaMeter. Without further model analysis, we can only detect the trend of a deepening cut-off low. Although the present period is generally drier than the past in the analogues, the change is not significant (figure 4.2 h). The present day analogues are warmer than the past but, again, however this is not significant (figure 4.2 i).

We assess the annual change in frequency of the most similar events. In the most similar 5% and 10% of events there is a statistically significant increasing trend through time (figure 4.3).
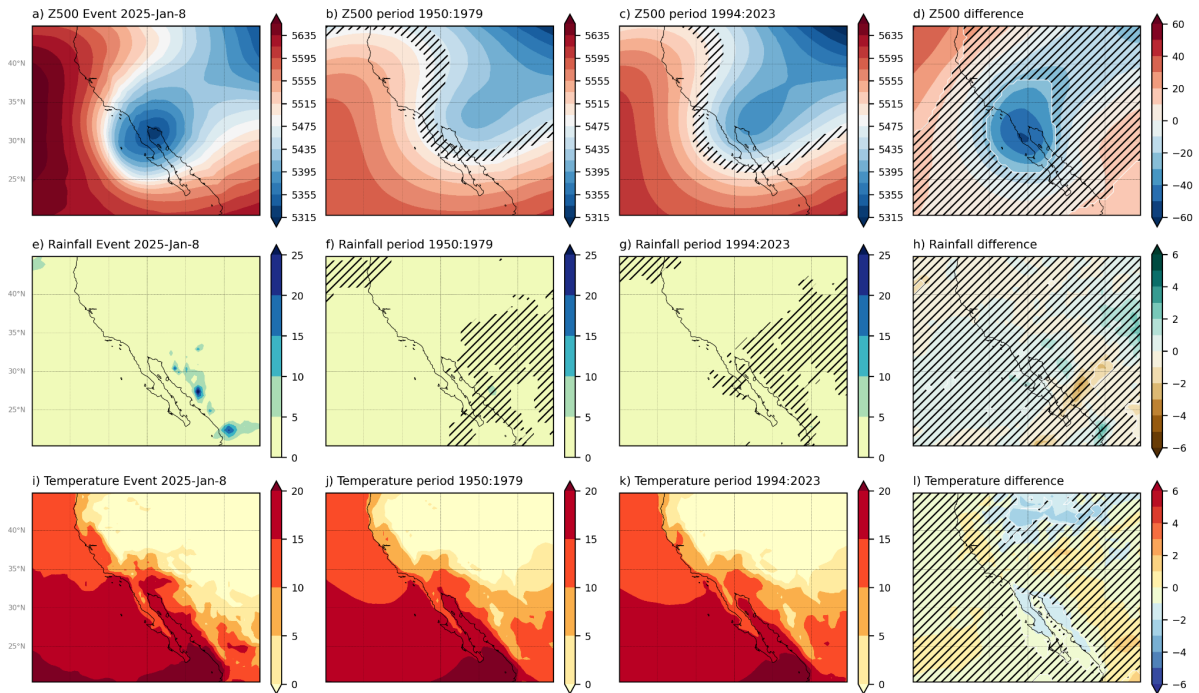
Figure 4.2: *Changes in atmospheric analogues. (a) 500hPa geopotential height field (m) for the event, 8 Jan 2025. b) Composite of the top 27 analogue days from the past period, 1950-1979. c) Composite of the top 27 analogue days from the present period, 1994-2023. d) Difference between the composites of past and present (present minus past). e-h) as in a-d for the rainfall field (mm). i-l) as in a-d for the 2m temperature field (°C). Z500 used to identify analogues in all plots. Hashing signifies regions where the signal is not significant based on a two-sided t-test.*

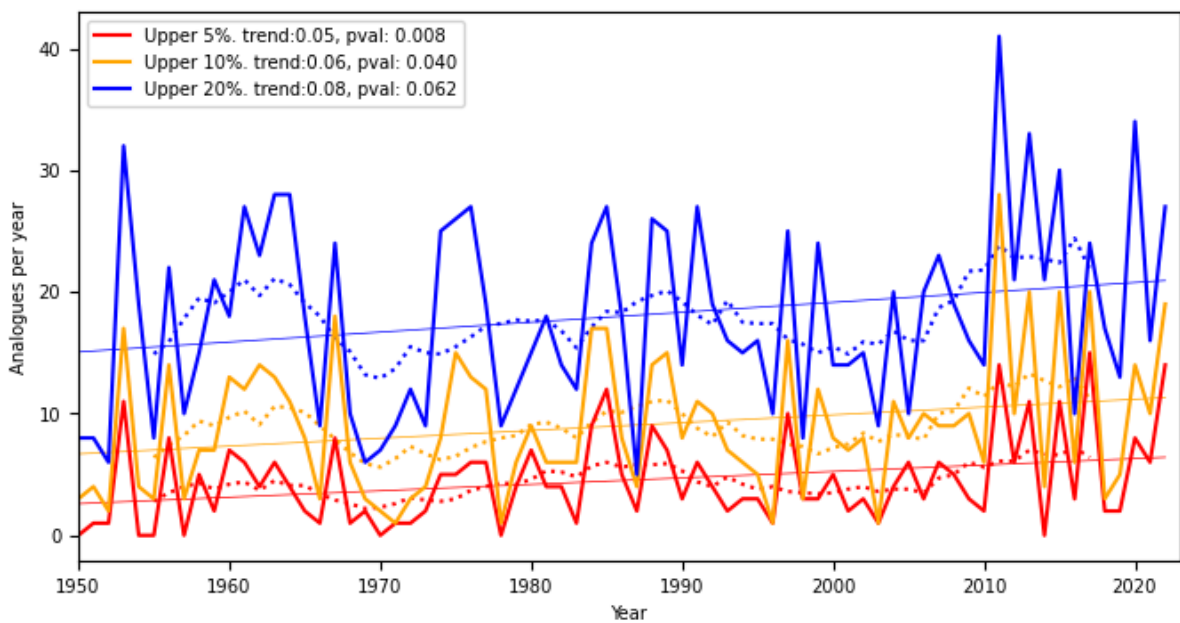***Figure 4.3*** *Trends in frequency of the most similar events. Number of "good" analogues per year (in DJF) at three threshold levels: the closest 5%, 10% and 20% of most similar days (based on Euclidean distance of Z500 field over the region [-130° to -100°E; 20° to 45°N]. Linear trend lines (solid thin lines) and multiannual trends (dotted lines) are plotted, with trend per year and p-value shown.*

Regarding the analysis of the simplified cut-off low index, the IC value obtained on 8 January 2025 is exceptional (-288 m) but not a record negative. The linear trend in the most negative Dec-Feb IC value per year from 1951–2025 is negative, but non-significant (figure 4.4 left). When analyzed using a GEV with a GMST covariate, we find that this value corresponds to a 19-year event [8-72 year]. The probability ratio for such an extreme, taken between 2024 and preindustrial period, using a covariate lowered by 1.3°C, is 2.5 [0.4-17], and therefore the increasing intensity of the extreme is not significant.

We further define the "occurrence of a COL" when IC<IC5, where IC5 is the 5-th percentile of the IC distribution in Dec-Jan, and we analyze the frequency of COLs. For a sensitivity analysis, we also used different percentiles as thresholds and different months, in particular Dec-Jan. Figure 4.4 (right) shows the annual frequency of COLs for Dec-Jan instead of Dec-Feb, for which the distribution of the geopotential height is more homogeneous. The frequency for Dec-Feb (resp. Dec-Jan) has a positive trend, which is not significant at the 5% level but would be statistically significant at the 10% level. . This trend corresponds to an increase of about 5% (resp. 8%) per decade, and the frequency has increased by about 50% (resp. doubled) since 1950.

Such a frequency trend is also found in all sensitivity experiments, by moving the location of the North-Western point P2 in a window of plus or minus 5° in the East-West direction and plus or minus 2° in the South-North direction (see box around P2 in Figure 4.1). Overall, positive trends are found within the range of 3%-6% per decade. We also find similar trends when considering the frequency of consecutive day events, instead of single day. However, even though we detect an increase in the COL frequency, it is impossible to formally attribute it to climate change without analysis of climate models, which is beyond the scope of this study. As for the trends found for analogues, it could be due to long-term variability.
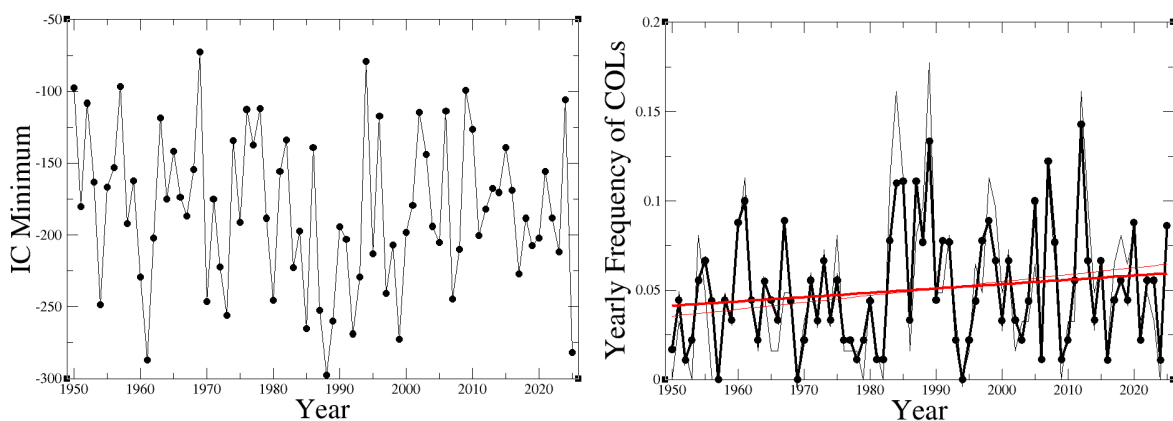

Figure 4.4. *Left panel: Yearly minimal values of the Dec-Feb IC index; Right panel: Yearly frequency of COLs, for the months of Dec to Feb (heavy) and Dec to Jan (thin).*

5 Climate change effect on modelled burned area

5.1 Data and methods

To attribute changes in burned area, we use the framework provided by the Inter-Sectoral Impact Model Intercomparison Project (ISIMIP) Phase 3a to analyse the impacts of climate change across different biophysical variables (Mengel et al 2021). Weather reanalysis products are detrended against global mean temperature changes since 1901, and atmospheric carbon dioxide concentration is fixed to early-industrial levels to create reanalysis-based climate counterfactuals, which are used in process-based biophysical models to simulate fires in a counterfactual world without climate change. These simulations are compared to fire model simulations with a factual climate. Here, climate change thus refers to observed long-term changes in climate variables irrespective of the forcing.

We follow the methodology described in Burton, Lampe et al. (2024) and use factual and counterfactual burned area simulations from seven ISIMIP3a fire models, forced by one factual and one counterfactual reanalysis-derived climate (GSWP3-W5E5) from 1901 to 2019. We compare the factual simulations with two satellite-based burned area observational products, GFED5 (Chen et al., 2023) and FireCCI5.1. Simulated burned area is available on a monthly time resolution and on a 0.5° spatial grid, with the observational products regridded to match the fire model's coarser resolution. We sum burned area over three different regions (California, Mediterranean California and Coastal Southern California, the latter corresponding to the study region used in Section 3, Fig 5.1) to obtain a monthly time series of burned area (in km^2) per region for each model/observational product. Then, we turn these into relative anomalies by subtracting the mean of each time series and then dividing by the mean (See Burton, Lampe et al., 2024). Subsequently, we calculate the RMSE and temporal normalized mean error (NME) between the relative anomalies of the observational products and each of the factual model-based simulations (See Table A3.1 for model evaluation metrics).
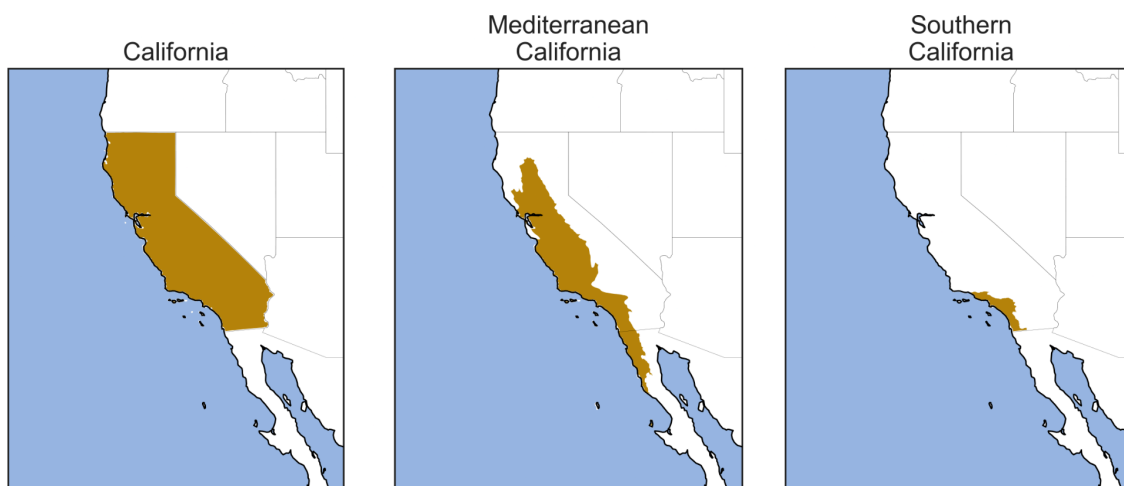

Figure 5.1*: The three regions used in this analysis. (i) The state of California (172 pixels in fire models), (ii) Mediterranean California (81 pixels); Level 1-2 ecoregion as defined by the United States Environmental Protection Agency and (iii) Coastal Southern California (US ecoregion 'Southern California/Northern Baja Coast'; 7 pixels), the study region used in Section 3.*

In the next step, we use the NME to weigh the models. We do this to give higher confidence to the models closely matching observations and to reduce the effect of models that struggle to capture the observed variability. To calculate weights for each model, we use Equation 5.1 (modified from Brunner et al. (2019)), where σ_D represents the strength of the weighing, with a lower σ_D meaning better-performing models will be most important in the final result. To find the optimal σ_D there exists no analytical solution, so we try 500 values between 0.001 and 10. Then, we create 1000 copies of our modelled relative anomaly time series for each model by adding in random noise scaled by the RMSE of each model. For each copy and each possible value of σ_D we calculate the weighted average and weighted standard deviation and calculate which fraction of the observations falls within the weighted average ± 1.96 weighted standard deviation. Subsequently, we apply a knee-point detection algorithm to find the optimal σ_D, i.e. lowest σ_D (strongest weighing) for which the largest fraction of the observations fall within the modelled spread.

$$Wi \;=\; e^{-\frac{Di}{\sigma D}}$$

Equation 5.1: *Formula used to weight the models. W_i is the weight for model i, D_i is the distance to the observations for that model (NME) and σ_D is a scaling factor. The lower σ_D is, the stronger the weighing will be i.e., more weight to the best model(s), the higher it is, the more purely democratic the ensemble becomes.*
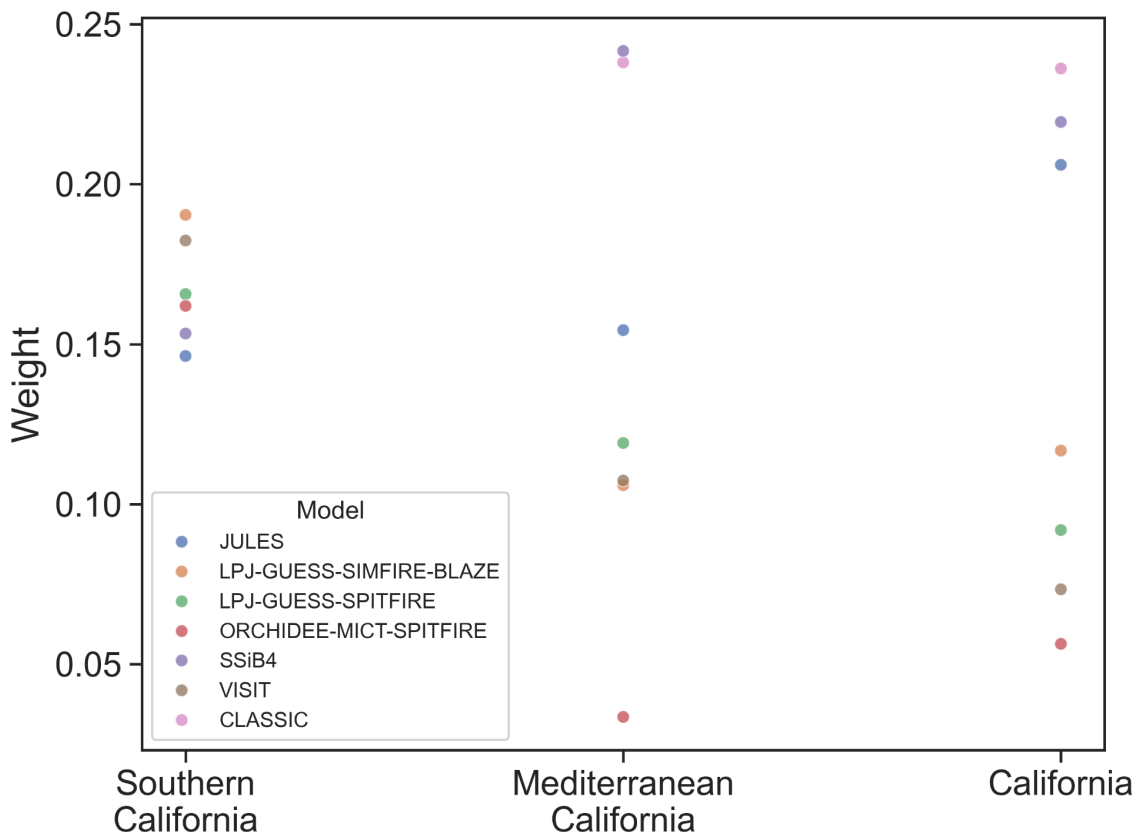
Figure 5.2: *Average model weights for the three selected regions. Note that CLASSIC was not used in Southern California as it modelled no burned area in any of the timesteps, making the calculation of relative anomalies impossible.*

To compare factual and counterfactual simulations, we create 1000 copies of each time series by adding in RMSE-weighted random noise to both factual counterfactual time series. We then calculate factual relative anomalies using the counterfactual mean as baseline, i.e. 'overburning', for each of the 1000 copies. Using the previously estimated optimal model weights, we resample 100000 'overburning' values for each timestep. ISIMIP3a reanalysis-based factual and counterfactual data is only available until 2019, so we present overburning results for this year, meaning values would be higher if the analysis were extended to 2024.

Figure 5.3: *Summary of the data flow in this setup (Burton, Lampe et al., 2024).*

5.2 Results

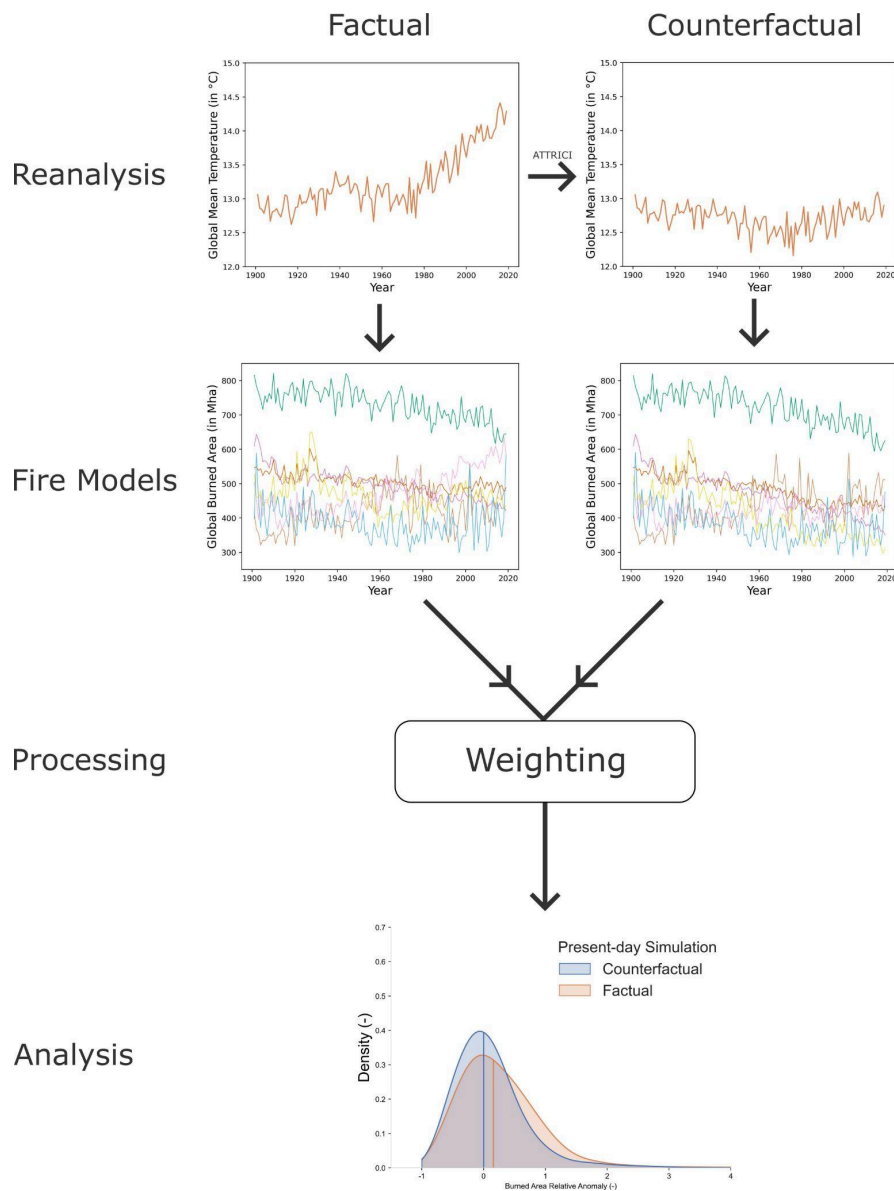These fire model simulations allow us to answer questions about expected trends in fire behaviour due to climate change in each region, during the historical period. This approach does not provide estimates about specific individual fire events such as the current ongoing fires. From these model analyses, we find that 'overburning', i.e. the increase in burned area under factual climate conditions relative to the counterfactual burned area without climate change, has steadily increased throughout the last 120 years (Turco et al., 2023). By 2019 we estimate annual burned area is 23.2% [0.1, 57.1] higher in factual climate conditions compared to what it would be under counterfactual climate conditions in California, 25.7% [3.5, 45.2] higher in Mediterranean California and 44.9% [5.3, 97.3] higher in Coastal Southern California (best estimate and 80% confidence interval). We calculate that based on the linear trend over the last 40 years, the overburning increases by 0.33% per year for California, 0.35% per year for Mediterranean California, and 0.54% per year for Coastal Southern California. Hence, for the end of 2024, our overburning best estimates of 2019 should have increased to 24.8% for California, 27.5% for Mediterranean California, and 47.6% for Coastal Southern California. We note that these represent the changes in burned area expected from the pure climate change effect, all other factors kept constant. In reality, fire management and other direct human forcings play a role. As these factors are not fully represented in the fire model simulations, observed trends in burned area can differ from the expected climate change effect.
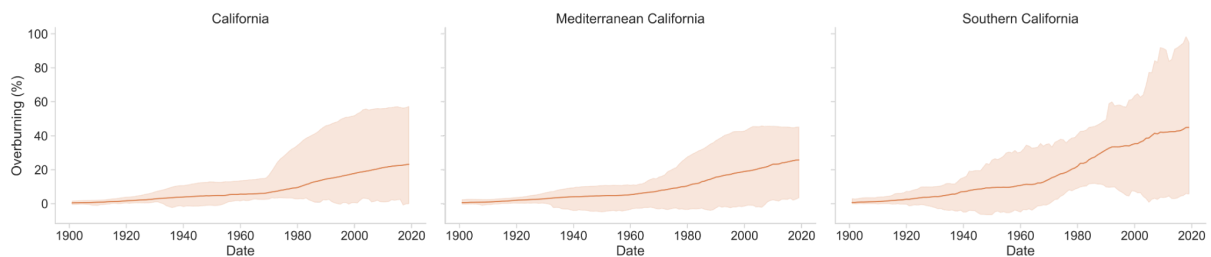

Figure 5.4: *Change in annual overburning from 1901-2019 in the different study regions.*
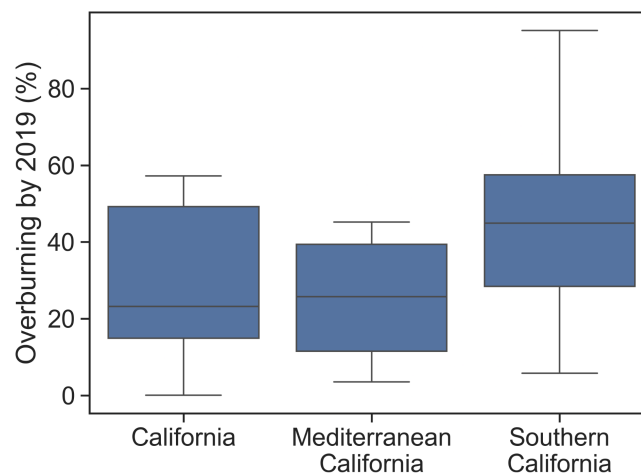

Figure 5.5*: Change in annual overburning by 2019, best estimate is the horizontal line in the blue box, the blue box represents the Interquartile range and the whiskers are the P10 and P90.*

We also analyse modelled changes in burned areas for only the months of December and January. These months normally represent only a small fraction of the total annual burned area, meaning relative changes (expressed in %) can more easily take on extreme high or low values compared to annual totals. Due to the larger uncertainty when looking only at these months, model responses show a larger spread, with uncertainty intervals including the possibility of no change in 2 out of 3 studied regions (Fig 5.6). The best estimates nonetheless all point to an increase in burned area under factual compared to counterfactual climate conditions. The models suggest that by 2019 burned area in December and January could be 17.3% [-43.8, 32.3] higher in factual relative to what it would be under counterfactual conditions in California, 9.1% [-28.0, 26.1] in Mediterranean California and 45.0% [12.7, 548.8] in Coastal Southern California.
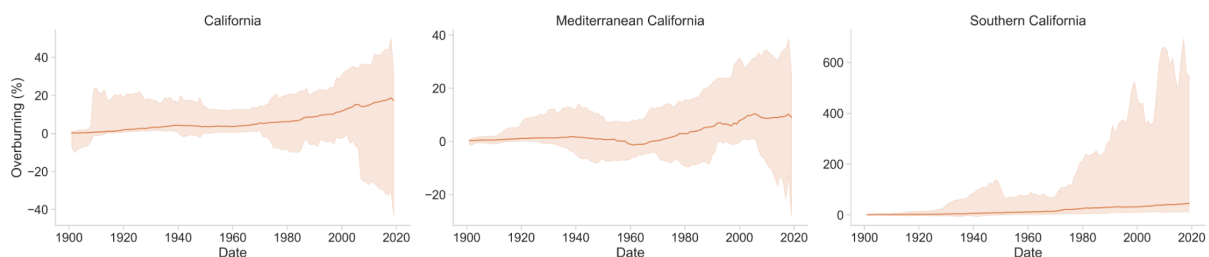
Figure 5.6: Change in December-January overburning from 1901-2019 in the different study regions.
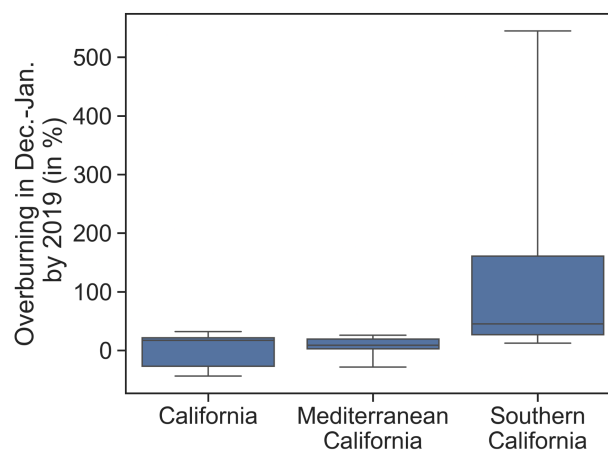
Figure 5.7: Change in December-January overburning by 2019, best estimate is the horizontal line in the blue box, the blue box represents the Interquartile range and the whiskers are the P10 and P90.

6 Summary of hazard synthesis

In sections 3-5 we examined several lines of evidence to understand the connection between climate change and the weather conditions associated with the devastating wildfires that occurred around Los Angeles in January 2025. While there is high uncertainty in the individual numbers reported, collectively these different analyses point in the same direction, indicating that the conditions conducive to extreme fire activity have become more intense and more likely to occur due to global warming, and will continue to do so with further warming.

Probabilistic attribution of trends in peak January fire weather indicates that the conditions on the day the fire broke out were unusual, but not unprecedented; similarly extreme values of the fire weather index are expected around once every 17 years in the current climate, but would have been expected to occur only once every 23 years in a 1.3°C cooler preindustrial climate, with observed January peak FWI now around 6% more intense than it would have been without global warming. We acknowledge that the uncertainty around these numbers is high, but this is not surprising: we are evaluating changes in the most extreme value of FWI in a single month (January) of each year, in a very small region where climatic variability is known to be particularly high. Nonetheless, the fact that the climate models simulate similar changes in FWI1X gives us confidence that the assessed changes are indeed a climate change signal. (Section 3.1)

Data		% intensity change (95% CI)	Probability ratio (95% CI)
Observations	Past- Present	6.26 (-10.8 - 34.4)	1.34 (0.44 - 4.8)
Models		5.33 (-10.2 - 22.7)	1.37 (0.51 - 2.9)
Synthesis		5.67 (-10.4 - 27.4)	1.37 (0.48 - 3.6)
Models only	Present- Future	3.22 (-5.9 - 10.5)	1.37 (0.51 - 2.9)

Table 6.1: Same as Table 3.2, reproduced for ease of reference. Synthesised reanalysis and model results for changes in FWI1X associated with increasing GMST, as presented in Figures 3.3 and 3.4. Statistically significant increases (decreases) in probability and intensity are highlighted in dark blue (orange), while non-significant increases are highlighted in light blue (orange).

The low rainfall recorded from October-December 2024 is also expected to occur around once every 20 years in the current climate, but would have been more unusual in a 1.3°C cooler preindustrial climate, being around 2.4 times more likely to occur in the present climate according to ERA5. The synthesis implies an increase of 61% in the likelihood of experiencing a similarly dry October-December period in 2024 compared to in a preindustrial climate, although the uncertainty ranges are again high. The CORDEX climate models used in the analysis, which are driven by CMIP5 global circulation models, do not agree on the signal of the change; however, the SST-forced HighResMIP models, which are part of more recent CMIP6 activity, simulate a similar trend to that observed in ERA5. This suggests that the observed drying trend is attributable to climate change, although the signal is not reproduced by the earlier generation of climate models. (Section 3.2)

Data		(c) All models		(d) HighResMIP only	
		Change in SPI (95% CI)	Probability ratio (95% CI)	Change in SPI (95% CI)	Probability ratio (95% CI)
ERA5	Past-Present	-0.36 (-1.2 - 0.4)	2.41 (0.33 - 20.9)	-0.36 (-1.2 - 0.4)	2.41 (0.33 - 20.9)
Models		-0.16 (-0.77 - 0.47)	1.26 (0.32 - 8.03)	-0.29 (-0.99 - 0.46)	1.88 (0.32 - 15.3)
Synthesis		-0.23 (-0.93 - 0.46)	1.61 (0.31 - 11.58)	-0.32 (1.07 - 0.44)	2.10 (0.32 - 17.6)
Models only	Present-Future	-0.06 (-0.44 - 0.31)	1.19 (0.45 - 2.65)	-0.27 (-0.93 - 0.43)	1.90 (0.33 - 6.17)

Table 6.2: *Same as Table 3.4, reproduced for ease of reference. Synthesised reanalysis and model results for changes in SPI-OND associated with increasing GMST, as presented in Figures 3.7 and 3.8. Statistically significant decreases in SPI / increases in likelihood are highlighted in dark orange, non-significant decreases in SPI / increases in likelihood are highlighted in light orange. (a) Synthesis of reanalysis with all climate models that passed evaluation; (b) synthesis of reanalysis with only HighResMIP models.*

A critical factor in the severity of the January 2025 fires was the arrival of strong Santa Ana winds before enough rain had fallen to wet the vegetation and suppress fire risk. To assess changes in the timing of drought-ending rains – and so to understand the changing risk of overlap between the dry season and the peak of the Santa Ana winds - we also analyse changes in the end of the drought season, defined as the single largest weekly drop in the drought code (a component of the FWI, see Section 3.3) each year. ERA5 records a delay of 23 days in the end of the drought season, which while not statistically significant at the 5% level would be significant at the 10% level. The climate models collectively exhibit no clear signal, and so we cannot confidently attribute the observed change to anthropogenic warming, nor do we attempt to project future changes in the timing. However, the timing of the drought end index is sensitive to how droughts and wetting periods are defined, and will also be sensitive to how well the climate models capture the seasonal cycle and temporal granularity of rainfall events, so the high uncertainty about these estimates and lack of agreement among the climate models are not surprising. Previous research has detected a delay of a similar length in the onset of the rainy season and found this shift to be consistent with projections of future climate across California (Goss et al., 2020; Lukovic et al., 2021; Swain, 2021; Dong et al., 2022) so we conclude it is likely that the observed trend toward a delayed end of the drought season was promoted by anthropogenic warming, but that due to the small size of the region evaluated in this study, we do not detect a consistent signal in the climate models in our analysis. (Section 3.3)

Data		Change in day of year (95% CI)	Probability ratio (95% CI)
Observations	Past- Present	22.7 (-2.7 - 49.1)	1.29 (0.97 - 1.8)
Models		-0.86 (-25.3 - 24.1)	1.14 (0.27 - 4.0)
Synthesis		10.4 (-14.6 - 36.1)	1.28 (0.84 - 1.97)
Models only	Present- Future	0.23 (-18.4 - 18.7)	1.14 (0.27 - 4.0)

Table 6.3: Same as table 3.6, reproduced for ease of reference. Synthesised reanalysis and model results for changes in the day of year on which the drought season ends, as presented in Figures 3.11 and 3.12. Statistically significant delays in the end of the season / increases in likelihood are highlighted in dark orange, non-significant decreases in SPI / increases in likelihood are highlighted in light orange. Rows corresponding to a change of less than 1 day are not shaded.

Alongside these probabilistic attribution analyses, we also consider trends in the occurrence of large-scale circulation patterns commonly associated with strong Santa Ana wind activity, using the so-called analogue method (Section 4). Winter days with similar circulation patterns to January 8th, which showed a strong cut-off low, are identified, and changes in the frequency of occurrence of similar patterns are analysed, along with changes in the atmospheric and weather conditions associated with similar patterns in the past (1950-1979), when the climate change signal was weaker, and in recent decades (1994-2023). This analysis finds that similar circulation patterns are occurring more frequently now than in the past, and that cut-off lows in this region are deeper in the present period than in the past, which would be expected to lead to stronger winds in the Coastal Southern California region. While these trends were found to be statistically significant, they cannot be formally attributed to climate change without analysing climate models, which is beyond the scope of this report.

Finally, we analyse simulations from process-based fire models run under observed and counterfactual climate conditions, to estimate the expected effect of climate change on burned area in the region. These models suggest that the potential burned area in December-January in the Los Angeles area is today substantially higher than it would be in the absence of climate change. These models represent changes in potential burned area in response to climate change and so do not faithfully reproduce observed trends in actual burned area, which are the combined result of climate change and direct human interventions in the landscape. (Section 5)

The Coastal Southern California region is a small area, often represented by only a few grid-boxes in climate models and gridded observational products. Furthermore, the complexity of the weather conditions characterising fire weather and large year to year variability in rainfall means that precise numbers in every single line of evidence are uncertain. The intensity of the severe wildfires in January 2025 were driven by extremely high wind speeds, for which reliable gridded observations are not available and which are not expected to be well represented in climate models, making direct attribution of this factor all but impossible and further increasing uncertainty in the results. However, the lines of evidence examined overall point in the same direction, indicating that conditions that make extreme fires more likely are becoming increasingly frequent and severe. This is also in line

with existing literature, as summarised by the IPCC (AR6 WGI, Chapter 12), that shows an increase in high temperatures combined with a drying in the wider area, and thus higher fire risk. Given all these lines of evidence we have high confidence that human-induced climate change, primarily driven by the burning of fossil fuels, increased the likelihood of the devastating LA fires.

7 Vulnerability & exposure

In the past decades, human and infrastructure exposure to large fires have increased significantly, especially in the western United States (Rad et al., 2023). The Los Angeles urban wildfires, which started on January 7, 2025, are among the most destructive of human property in Southern California's history. As of January 23, the Palisades Fire has consumed over 23,448 acres, and the Eaton Fire has burned approximately 14,000 acres (WatchDuty). Collectively, these fires have resulted in at least 28 fatalities and destroyed more than 16,000 structures (LA County Medical Examiner, Cal Fire Eaton, Cal Fire Palisades). The fires' proximity to densely populated urban areas has resulted in their significant impact. They are, however, well within the range of fire size recorded historically for southern California chaparral ecosystems (Keeley and Zedler 2009). The ignition of the fires is under investigation but has a high likelihood to be human-caused based on the rarity of lighting and proximity of the two ignition points to human infrastructure.

The wildfires have also significantly deteriorated air quality across the Los Angeles region. PM2.5 levels—a measure of fine particulate matter harmful to health—have reached the "Unhealthy" Air Quality Index (AQI) category or higher in areas such as Altadena, Downtown Los Angeles, Malibu, Pacific Palisades, and Pasadena. The combination of hazardous air quality and the fires' proximity to urban centers highlights the unique vulnerabilities and impacts faced by densely populated Los Angeles areas during such environmental disasters.

This section looks at the exposure, the people and places in the path of the wildfires and smoke, and the vulnerability, the underlying factors that may have worsened or ameliorated the impact of the fires. In addition to exposure, we explore air quality, fire risk management, water systems and policy and legislation in order to develop an understanding of the complex human systems in place that interfaced with the wildfires.

In doing so, it's important to put this wildfire in the context of past impactful wildfires. Wildfires affect southern California or Los Angeles almost every year. For example, in 1961, the Bel Air fire destroyed 484 homes and damaged 190. The fire led to improvements in policies to reduce risk in case of future fires by enacting building code upgrades such as banning wood shake/shingle roofs, and creating the Brush Clearance program (LAFD Museum, LAFD). The Bel Air fire was also extremely fast to grow and spread as a result of the strong Santa Ana winds. In 1978, the Mandeville fire burned much of the area included in the eastern portion of the Palisades Fire. More recently, in November 2018, the Woolsey fire burned over 90,000 acres in LA and Ventura counties, killed 3 people and destroyed over 1,500 structures (NPS). It also led to the evacuations of about 300,000 people. In an after action review by LA County after the fire, the county recognised the fire department for its

preparedness before the strong dry wind event, and early recognition of the need for an unprecedented evacuation operation, while also recommending improved communication and upgrade alert systems to ensure timely communication during future wildfires (AA Review). In the context of the hazard attribution findings of this report, the increased risk of fire weather points to the need to learn from this disaster and past wildfires to be better prepared for the future.

7.1 Exposure

Both the Palisades Fire and the Eaton Fire burned through almost entirely chaparral vegetation, which is composed of evergreen, sclerophyllous vegetation typical of a Mediterranean-type climate of hot, dry summers and cool, wet winters. Plants are typically 1–3 m, forming dense thickets without an understory when mature. Fire return intervals are typically 40-130 years for pre-European colonization conditions and large fires are a normal occurrence based on the inherent characteristics of the vegetation and landscape (Keeley and Zedler 2009). Within the natural fire periodicity, burning poses no harm to the ecosystem, and the vegetation has many adaptations to recover after fire, including crown sprouting, bulbs, and smoke-stimulated seeds (Keeley and Fotheringham 1997). In more moist areas, evergreen oaks are dominant and create an emergent canopy with shrub understory.

The Los Angeles region has been home to Indigenous peoples since around 10,000 years ago, as the region emerged from the Younger Dryas cool period. With staple foods including oaks, walnuts, and chia seeds, they used fire to manage the landscape to promote growth of oaks and grassland annuals. Fire was also used to clear out areas for hunting, along travel routes, and near important landscape resources such as springs. Although early Spanish missionaries report extensive cultural burning along their paths, no evidence suggests that entire steep mountainsides were intentionally burned, but rather were low-intensity summer/fall burns to promote herbaceous growth or at a fine scale to manipulate local conditions (Anderson 2005, Lightfoot and Parrish 2009).

The Spanish colonized a landscape with an existing fire regime modified by Indigenous practices (Ethington et al. 2020). They converted the land use to ranching and began efforts to stop Native burning, which were continued after statehood in 1850 (Minnich 2008). As land uses shifted to ranching, agriculture, and then industry and rapid growth and urbanization following the transcontinental railroad, fire in the hills and mountains was commonplace, and large fires (>10,000 ha) were a regular occurrence and even very large fires (>50,000 ha) documented, all through predominantly chaparral vegetation (Keeley and Zedler 2009). The plains and valleys of the Los Angeles Basin have been urbanized, along with the riparian zones and wetlands characteristic of the lowlands. Development has pressed into the chaparral-covered hillsides, starting with hunting cabins, and followed by small scale and large scale residential developments. In two of the fire perimeters, residential communities were established, located at the flatter foothills and terraces at the base of mountains. Altadena was established in the 1880s, expanding out through former vineyards and orange groves at the base of the San Gabriel Mountains and Pacific Palisades in the 1920s at the base of the Santa Monica Mountains (Zack, 2012). In the 1970s, the Palisades Highlands was built as a development in the hills above the Palisades completely surrounded by chaparral and bringing an associated wildland trail system and infrastructure.

As with all Mediterranean-type ecosystems, fires typically occur in the late summer and fall, extending into the winter months until rainfall has restored vegetation moisture. Large fires correspond with mountain winds (Santa Ana winds), which typically occur between October and April (Guzman-Morales et al. 2016), meaning the highest fire risk is between October and the onset of substantial winter rains, whenever that occurs. Earlier season fires (e.g., summer) are associated with drought conditions, but 2024 had high rainfall and vegetation moisture was higher than usual through the end of September (see https://fire.lacounty.gov/wp-content/uploads/2025/01/Los-Angeles-Basin-Graph.pdf). Vegetation moisture reached critical levels in October and stayed there through the January fire events.

Both fires consumed fuels in areas that had burned at least once since 1900 for the majority of their extent (Figures 7.1 and 7.2). These areas encompassed low-density residential areas in the City of Malibu and Topanga Canyon region of Los Angeles County for the Palisades Fire. Higher density residential areas built within post-1950 fire footprints also burned, namely portions of the Palisades Highlands. Both fires also reached and then burned into densely built single family neighborhoods and associated commercial and institutional zones – the village of Pacific Palisades and the community of Altadena – areas that had not burned since 1900 (but certainly burned in wildfires before urbanization). Within these areas, the fires were largely not spread by vegetation, but rather by embers and radiant heat from structure to structure (LAist, 2025). The extreme winds precluded any air support during the first day of the fire, leaving firefighters unable to control an urban conflagration fueled by excessive winds.
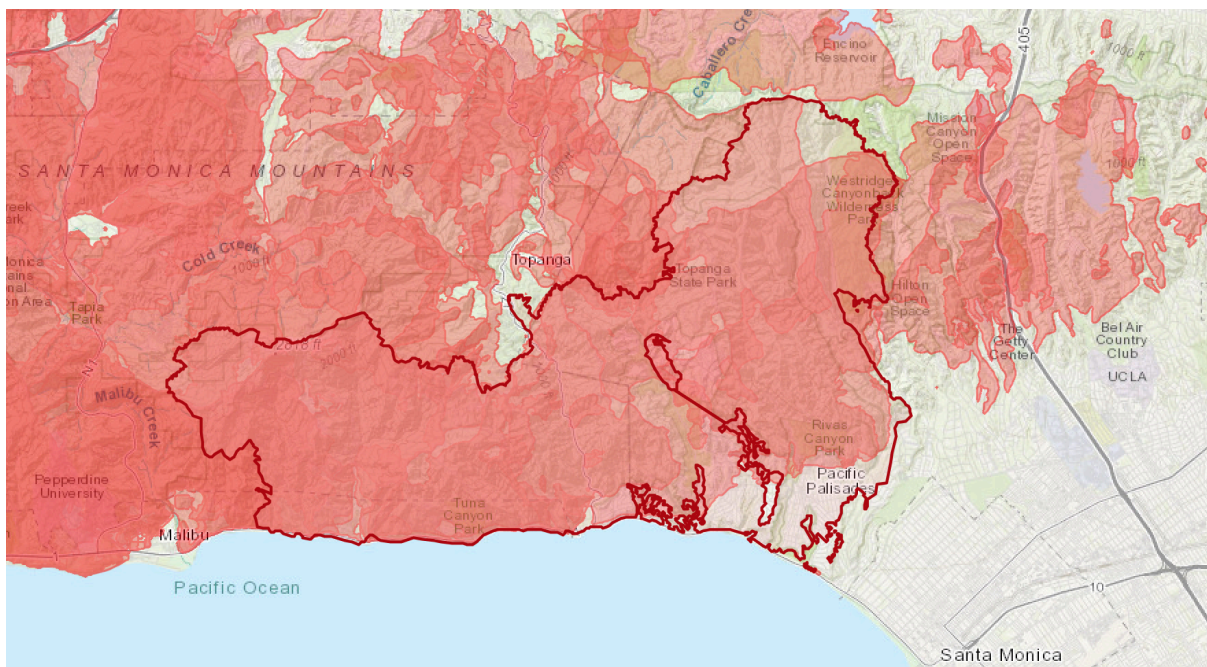
Figure 7.1. Palisades Fire perimeter relative to all fires recorded since 1900. Red shades represent fire events. Darker colors represent overlapping fires in the historical record. Data from Cal Fire; visualized in ArcGIS Online.
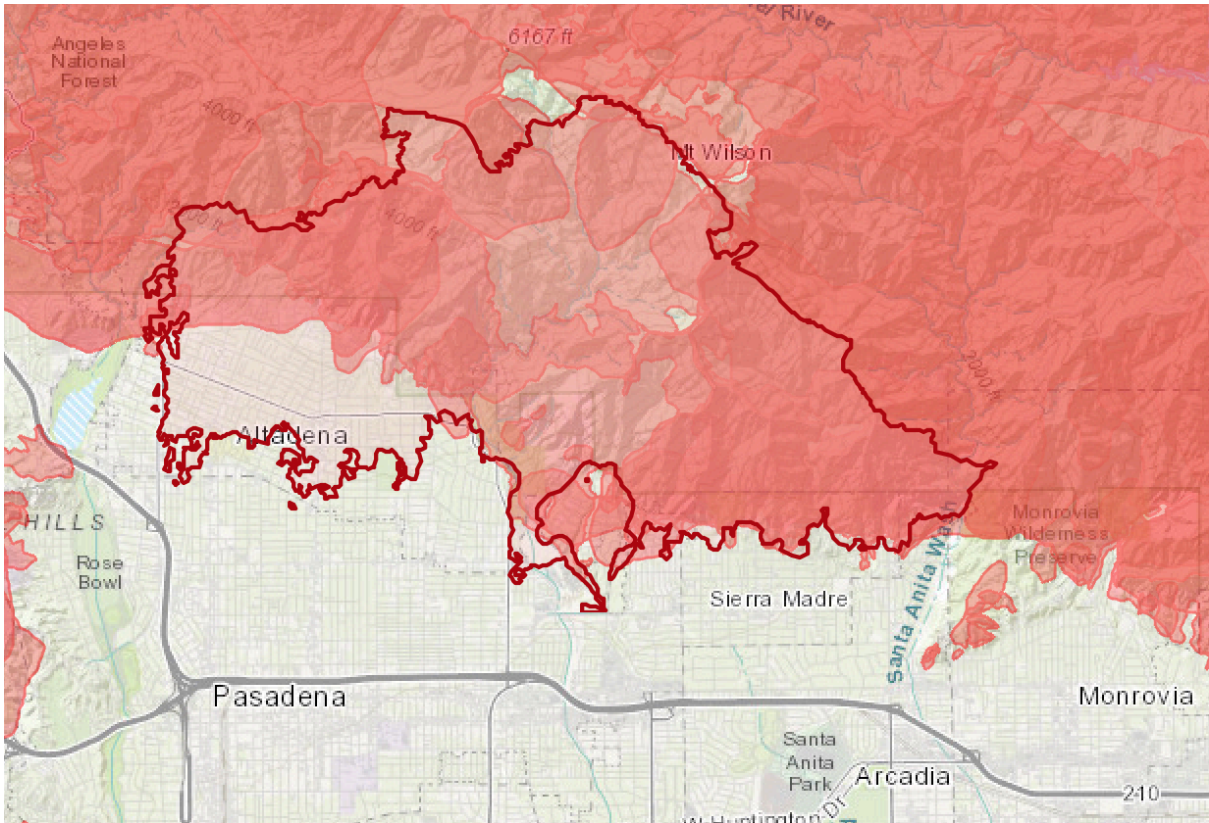
Figure 7.2. Eaton Fire perimeter relative to all fires recorded since 1900. Red shades represent fire events. Darker colors represent overlapping fires in the historical record. Data from Cal Fire; visualized in ArcGIS Online.

All of the Palisades Fire footprint was within the Very High Fire Hazard Severity Zone, so all structures should have had required defensible space and vegetation management within 200 ft (City of Los Angeles). Post-fire assessments may reveal the degree to which these requirements were followed. The Eaton Fire, in contrast, extended well into neighborhoods that were not within the mapped VHFHSZ and therefore had no required vegetation management or defensible space regulations (Figure 7.3). The VHFHSZ corresponds closely with documented wildfires since 1900.
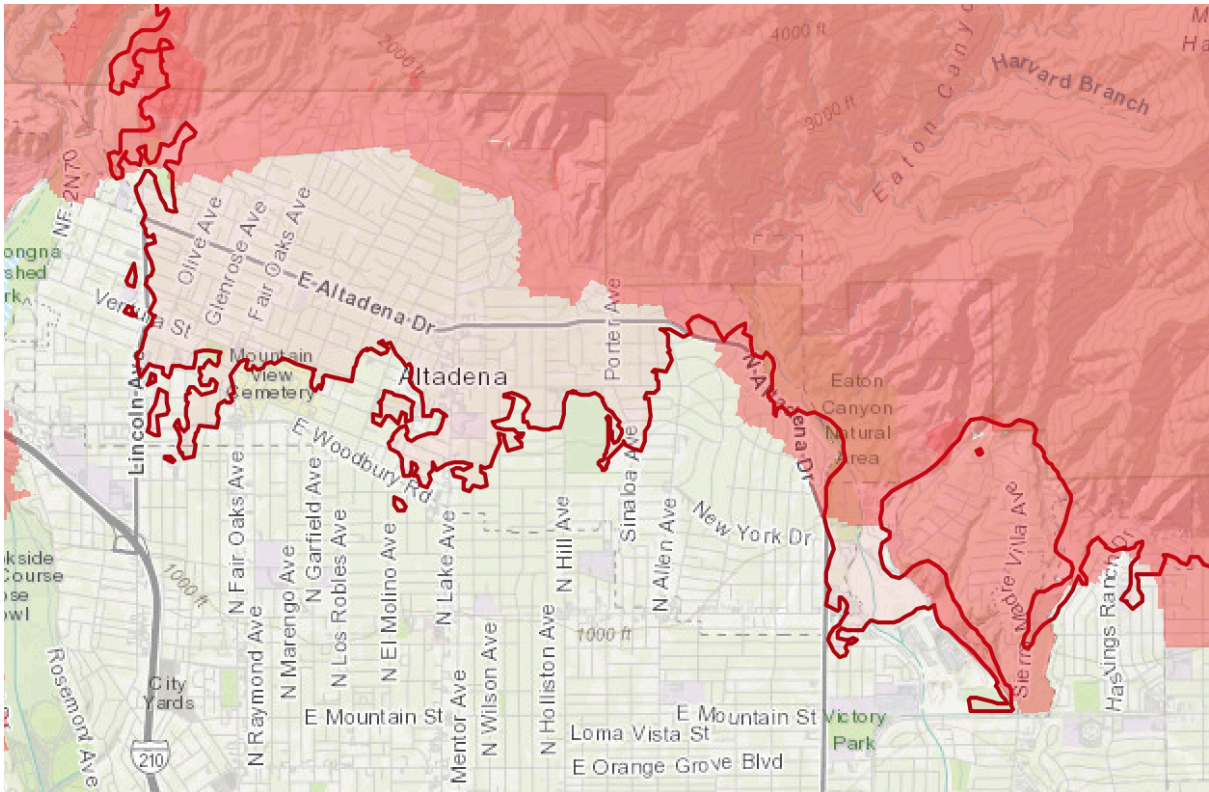
Figure 7.3. Zoomed in Eaton Fire perimeter (red outline) with the extent of the Very High Fire Hazard Severity Zone (red shading).

7.2 Fire risk management

7.2.1 Prevention

Prevention remains a cornerstone of fire risk management, shaping strategies from early detection systems to targeted fuel reduction near structures and infrastructure (Ready.gov, n.d.). In 2025, early warning and response measures in Los Angeles relied on satellite-based fire detection (NASA FIRMS, n.d.) and automated weather stations (NWS, n.d.) to identify ignition hotspots.

The 2025 wildfires were driven by hurricane-force Santa Ana winds reaching speeds of up to 100 mph, which played a critical role in the rapid fire spread and extreme fire behavior. Over 200,000 residents were under evacuation orders (NBC News, 2025), and first responders faced immense challenges due to the speed and unpredictability of fire movement.

Fuel availability was exacerbated by drought conditions, low humidity, and vegetation build-up from the previous winter. While chaparral ecosystems do not support undergrowth in the traditional sense, fire risk in these environments is impacted by fine fuels such as seasonal grasses and invasive weeds within designated fuel management zones. Los Angeles City and Los Angeles County ordinances encourage property owners to clear defensible space (Public Resources Code §4291, 2021; Los Angeles County Code Title 32, 2019; City of Los Angeles Fire Code Chapter 49), and both the City

and County fire departments mail Annual Brush Clearance Notices to residents in the Fire Hazard Severity Zones (FHSZs) and has integrated a geospatial database into the Defensible Space Inspection Program to improve accuracy ([LAFD, 2024](#); [LAFD, n.d.](#)). Over time, broader land-use changes, such as the expansion of residential developments deeper into wildland areas, have also intensified wildfire vulnerability ([Radeloff et al., 2018](#)). While the availability of fuel is a factor, the intense wind conditions and ignition source was the major driver of the wildfire.

To mitigate wildfire disasters, Los Angeles has implemented several proactive measures. The "Ready! Set! Go!" Wildfire Action Plan emphasizes public preparedness and evacuation readiness ([CAL FIRE, n.d.](#)). Additionally, the city has augmented staffing and pre-deployed resources during high-risk periods, enforced parking restrictions on "red flag days," mandated vegetation clearing with regular inspections, and developed "ember-resistant zones" near structures to reduce ignition risks ([City of Los Angeles, 2021](#); [Stewart, 2024](#); [Beverly Hills, n.d.](#); [Kensington Fire, n.d.](#)).

The Community Wildfire Protection Plan (CWPP) can be a key component to managing wildfire risks, particularly in the Wildland-Urban Interface, however, only part of the areas burned by the Palisades Fire had an adopted CWPP. Given that wind speed is three times more influential than vegetation moisture in driving extreme fire behavior ([Clark et al., 2008](#)), integrating these mitigation strategies with improved evacuation coordination and continuous assessment of vegetation changes will be critical for reducing future wildfire threats ([Ready.gov, n.d.](#)).

7.2.2 Response

Over 300 firefighters and 135 engines were pre-positioned in LA, but the exponential spread of four fires and strong winds overwhelmed resources ([Axios, 2025](#), [Governer's Office, 2025](#)). As of January 24th 2025, over 16,000 personnel, including National Guard members and firefighters, are responding with 2,000+ equipment pieces, 1,490+ engines, and 80+ aircraft ([Governer's Office, 2025](#)). Despite a 7% budget increase, LA's fire department remains underfunded, with less than one firefighter per 1,000 residents ([CNN, 2025](#), [Carbonbrief, 2025](#)). County firefighters and 1,000 trained incarcerated people bolster operations, though their participation raises concerns about coercion, disproportionate injury risks, low pay, and the long-term health implications ([ABC news, 2025](#), [Times Magazine, 2018](#), [Forbes, 2025](#), [The Marshall Project 2025](#)). To mitigate health impacts, over 1 million masks and clean water were distributed, and shelters mobilized additional emergency units ([Governors Office, 2025](#), [County of Los angeles, 2025](#)). However, overwhelmed health services face a months-long recovery ([Rosenthal, Stover and Haar, 2021](#)).

The response was facing challenges including water shortages from hydrants ill-equipped for prolonged high demand ([Reuters, 2025](#), [The Conversation, 2025](#)). The wireless emergency alert system was used to notify residents in the path of the fire to evacuate, though some arrived late ([CNN, 2025](#)). Road blockages and traffic congestion of major evacuation routes slowed down evacuation efforts and delayed emergency vehicles, requiring bulldozers to clear abandoned cars ([BBC, 2025](#)).

Evacuations also struggled with identifying vulnerable communities due to reliance on biophysical risk assessments resulting in insufficient use of various communication channels and inadequate multilingual alerts ([Ermagun et al., 2025](#), [Méndez, Flores-Haro and Zucker, 2020](#)). Wealth, age, disability, and language are factors that affect vulnerability to wildfires, and may result from

inaccessible warning systems and communications, barriers to quick mobilisation for evacuation, and societal inequities in access to insurance against damage (The Conversation, 2023). One of the main challenges is that fires are fast spreading, so timely evacuation is crucial. While 200,000 evacuated successfully, vulnerable groups such as elderly, people living with disability or population groups that received late warnings, lagged behind (NBC News, 2025, CNN, 2025). Additional linguistic barriers and geographical disadvantages for some groups compound with immobility (Hopfer et al., 2024, Baker et al., 2024). The elderly, people with disabilities, caretakers, the unhoused, and people from lower socioeconomic backgrounds without personal vehicles face heightened evacuation difficulties (Ermagun et al., 2025, Backer et al., 2021, Ermagun and Janatabadi, 2024). Prior to the January 2025 fires, in the Pacific Palisades evacuation zones approximately 4,000 people lacked vehicle access, 6,000 lived with disabilities and 17,000 were over 65; in Eaton, these figures were ca. 2,000, 8,000, and 22,000, respectively (Department of Forestry and Fire Protection, 2025, 2025). Free public transport and car sharing were offered but were hindered by road blockages (County of Los Angeles, 2025). Impacts could result in death, with affected people being disproportionately elderly or people with disabilities, with reports highlighting that some were waiting to be evacuated (CBS news, 2025). In Altadena, a neighbourhood west of Lake Avenue, a formerly redlined area with high African American homeownership received warnings that were delayed compared to the other affected neighbourhoods and 17 people died in the area (Fahy, 2025). Reasons for the delay are under investigation (LA Times, 2025).

Access to emergency shelters remains a concern, particularly for people with disability, elderly, ethnic minorities given the continuation of care, physical access and distance, and availability of shelter information. Moreover, LA has one of the lowest shelter densities nationwide, (Ermagun and Janatabadi, 2024). Only six shelters are open, the majority closer to the wealthier Palisade area, meanwhile discounted hotel or Airbnb rates remain unaffordable for many (Governor's Office, 2025, CN Traveler, 2025). With limited shelters, high displacement and homelessness, large parts of the population have little room for coping, leaving them exposed to dire financial situations and health implications (Urban Institute, 2025, The Homeless Initative, 2025, LA times, 2025).

7.2.3 Community coping capacity

Recent wildfires in Los Angeles have once again tested the resilience and coping capacity of communities in their path.

Neighbors came together to assist each other, providing shelter, food, and emotional support to those who had lost their homes (CNN, 2025; PBS, 2025). For example, within 48 hours local residents set up relief centres for 500 displaced people and distributed over 10,000 meals (NY Times, 2025). Local organizations and charities swiftly mobilized resources, set up relief centers, and distributed essential supplies (CNN, 2025). Companies like Uber and Lyft provided free rides to shelters, AirBNB offered some free housing to displaced people, UHaul is offering 30 days of free self-storage and restaurants are offering free meals (KTLA5, 2025). Social media became a vital tool for coordinating efforts, sharing information, and connecting people for mutual aid efforts (Watchtendorf and Kendra, 2025).

The fires led to the evacuations of tens of thousands of people, with over 15,000 looking for space in emergency shelters (KTLA5, 2025). As of January 24th 2025, the American Red Cross 'had provided more than 11,300 overnight stays in shelters and, with our partners, more than 102,000 meals and snacks.' In addition nearly 22,000 relief items had been provided such as cleaning supplies, face masks, flashlights, gloves and other essentials (Red Cross 2025). With the cost of housing and rent prices already high, some displaced residents have temporarily moved in with family and friends in LA and beyond (CNN, 2025). For many Black residents in Altadena, their homes were their major source of generational wealth, and therefore with uncertain insurance coverage, the Eaton fire could dramatically affect their socio-economic status and ability to cope with future shocks and stresses (The Guardian, 2025; CNN, 2025). Furthermore, the wildfires are also a major source of stress and anxiety for those who faced them, with mental-health crisis centers seeing an increase in calls (Time, 2025).

7.2.4 Recovery and adaptation

Immediate responses in the aftermath of the LA wildfires include substantial support by the California Health and Human Services Agency, providing food, water, shelter, and healthcare to impacted populations (CBS, 2025). Discussions on how to rebuild while mitigating the impacts of future wildfire risk have begun to take shape around expanding building code traditionally reserved for the WUI to more urban and low- or moderate-risk fire zones (WJBF, 2025). While exact numbers of people covered by fire insurance in the affected areas are not available, the recent flight of insurance companies like State Farm from parts of California implies that there may be a portion of the population that is under-insured or uninsured, potentially making it difficult for many to rebuild (CBS 2025; Flavelle, 2025).

Recovery from wildfire disasters raises critical questions: who will rebuild, where will rebuilding occur, and through what means? Pre-existing disparities often influence new housing landscapes, with implications for displacement and homeownership (Lambrou et al., 2024). The increase in absentee ownership and the conversion of long-term rentals into vacation or short-term rentals may also result in a shortage of housing, driving up rental prices and preventing residents from returning to impacted communities (Weber et al., 2020; Peacock et al., 2014). Compounding these issues is that when it comes to post-disaster finance in the United States, owner-occupied properties are given priority, whereas repairs for rental units are much less common (Zhang and Peacocke, 2009), leaving tenants at greater risk of displacement.

Insurance challenges further complicate recovery efforts, as major companies have reduced wildfire coverage in California, leaving residents reliant on the state's FAIR Plan which offers limited protection at higher costs. Between 2020 and 2022 insurance companies declined to renew 2.8 million homeowner policies in California, while policies under the state's insurer of last resort, the FAIR plan, more than doubled in the last 4 years (EuroNews, 2025). The FAIR plan has 377 million in reserves to payout claims, while total losses from the wildfires are estimated to be in excess of 30 Billion USD potentially bankrupting the insurer of last resort and having implications for insurance availability in the state going forward (Favelle, 2025). The emotional, financial, and physical health of impacted populations persist as needs that are unmet through recovery funding schemes (Rosenthal et. al., 2021;

CBS 2025). These recovery challenges are especially prevalent for the Altadena neighborhood impacted by the Eaton Fire, whose demographic was diverse and middle-income, with household wealth built through multi-generational homeownership.

Managed retreat—meaning a planned and purposeful relocation of people away from hazardous locations—has gained popularity especially for flood-prone areas, though it is also associated with the risk of socially unjust community relocation initiatives (Koslov, 2019). Its application for wildfires is the subject of research, but largely absent in practice and applying the same framework as for floods could be maladaptive (Koslov, 2019). California's Governor recently issued an executive order aimed at expediting recovery by streamlining permitting processes for rebuilding, which may be a strong first step but continues to privilege homeownership, as well as those who are able to secure funding and resources (CA Gov, 2025).

7.3 Water systems

The 2025 Los Angeles wildfires exposed vulnerabilities in the city's water infrastructure and emergency response systems, underscoring the need for improved resilience, climate adaptation, infrastructure adaptation, and emergency preparedness. The primary challenge was the water system's ability to meet the extreme demands of large-scale wildfires.

Los Angeles' water infrastructure, designed for routine structural fires, struggled under unprecedented demand, four times the normal level for 15 consecutive hours, leading to localized shortages (Cercone & McCullough, 2025; Kane, 2025; Strupp, 2025). Pressure drops were particularly severe in elevated areas like Pacific Palisades, where the Santa Ynez Reservoir was unavailable due to ongoing repairs (Shamim, 2025; Goldin & Peterson, 2025). Further, about 20% of hydrants failed during firefighting efforts, further complicating containment operations (Goldin & Peterson, 2025).

The affected area also faced challenges with infrastructure upgrades. For example, in Malibu and Topanga according to reporting by the LA Times, "Many projects on a list of about three dozen 'highest priority' upgrades compiled by county officials in 2013 have yet to break ground in communities devastated by the fires. The County wrote that the upgrades would achieve 'critical goals,' including ensuring the system had enough water to meet 'fire flow needs.' The estimated cost was less than $57 million and construction would have taken about seven years." (LA Times 2025) Critical infrastructure included: water tanks, pumping stations, water lines and links to neighboring systems. In the same article though, a local public works official indicated that the fire system was designed for individual home fires, not wildfires, and thus operated as planned, he also indicated that the cited upgrades would have had marginal impacts due to the scale of the fires. Water system failures are also consistent with previous wildfires that have spread to urban areas such as the Maui wildfires in 2023 and Santa Rosa fires in 2017 (NY Times 2023, Prevention Web 2023)

Weather and climate conditions exacerbated these challenges. Severe drought and hurricane-force Santa Ana winds increased wildfire risks and hindered aerial firefighting efforts (NPR, 2025; de Puy Kamp et al., 2025), highlighting the need for long-term adaptation strategies.

Beyond immediate response limitations, the fires emphasized the importance of proactive infrastructure improvements. Water systems in wildfire-prone regions must be designed to handle

large-scale events, requiring investments in storage capacity, pressure management, and emergency reserves. Expanding the use of recycled water for fire prevention and suppression could also enhance sustainability (Portico, n.d.). Further, post-wildfire water quality concerns, such as increased sediment and contaminants, necessitate stronger monitoring and treatment measures (Wandersee et al., 2023).

Addressing these challenges requires collaboration among public agencies, utilities, and local communities. Strategic investments in resilient infrastructure, climate-adaptive strategies, and emergency planning will be critical in preparing for increasingly severe wildfire threats.

7.4 Air quality

In response to deteriorating air quality due to the wildfires, residents have been advised to stay indoors, use air purifiers, and wear N95 masks when outdoors to mitigate exposure to the harmful smoke. Major populations are affected, particularly vulnerable groups such as children, the elderly, and individuals with pre-existing respiratory conditions like asthma. The Los Angeles County Department of Public Health has declared a local health emergency due to the critical fire events, deteriorating air quality, and ash deposition, underscoring the heightened health risks for these populations (LA County, 2025). Additionally, the fires have led to the closure of public schools in several counties, disrupting daily life for thousands of families (LA County, 2025).

Satellite observations during the 2025 Los Angeles wildfires show dense smoke plumes reaching downwind population centers (Figure 7.4). Wildfire smoke, containing high levels of fine particulate matter ($PM_{2.5}$) — particles no larger than 2.5 micrometers in diameter — can travel long distances and significantly impact the surface air quality. $PM_{2.5}$ is well-documented as a health hazard due to its ability to penetrate the lungs and bloodstream, causing harm to the cardiovascular and respiratory systems. Toxicological and epidemiological studies suggest that short term exposure to wildfire smoke $PM_{2.5}$ is more toxic than an equal dose of ambient $PM_{2.5}$ (Wegesser et al., 2009; Aguilera et al., 2021). Exposure to wildfire smoke $PM_{2.5}$ is associated with all-cause mortality (Zu et al., 2016; Kollanus et al., 2016; Park et al., 2024), as well as respiratory morbidity, including asthma exacerbation and chronic obstructive pulmonary disease (COPD) (Alman et al., 2016; Kollanus et al., 2016; Vicedo-Cabrera et al., 2016; Stowell et al., 2019). For example, some studies have found that the 2018 Camp Fire led to several hundred respiratory hospitalizations within exposed areas, with for example 194 (95% CI: 78, 309) hospitalizations in Fresno County only (Letellier et al. 2024).

Additionally, wildfire smoke adversely affects mental health (Eisenman and Galway, 2022; Zhang et al., 2022; Wettstein et al., 2024), birth outcomes, including preterm birth and low birth weight (Holstius et al., 2012; Heft-Neal et al., 2022; Requia et al., 2022; Ha,et al., 2024), and can worsen respiratory infections such as influenza and COVID-19 (Landguth et al., 2020; Zhou et al., 2021). Besides short term effects, recent evidence also highlights the potential effects due to long-term and repeated exposures, including on incident dementia (Elser et al. 2024).

In addition to $PM_{2.5}$, wildfire smoke contains carbon monoxide (CO), nitrogen dioxide (NO2), and volatile organic compounds (VOCs) such as benzene and formaldehyde, which are carcinogenic (Wentworth et al., 2018). Certain populations are potentially at greater risk due to smoke pollution exposure, including outdoor workers (disproportionately impacting minority ethnic communities),

individuals with preexisting conditions, children, pregnant women, and the elderly (Cascio 2018; UCLA Latino Policy and Politics Institute, 2025).

The 2025 Los Angeles wildfire smoke may contain higher levels of toxic elements, such as heavy metals, compared to the burning of forests or other biomass. This is likely due to the combustion of plastics, chemicals in homes, properties, and vehicles. During the 2018 Camp Fire in Paradise, California, which destroyed over 18,000 structures, significant increases in lead and zinc were detected downwind (Yale Climate Connections, 2025; California ARB). As of January 23, 2025, over 16,000 structures have been destroyed in the Palisades and Eaton Fires in Los Angeles (CAL FIRE, 2025). Early measurements taken miles downwind from the Los Angeles wildfires showed that concentrations of atmospheric lead, a neurotoxin, reached 100 times the average levels, and chlorine, also toxic at low concentrations, reached 40 times higher than average (ASCENT data). Lead is commonly found in paint and pipes in older homes, while chlorine and other chemicals are released when plastics melt or burn (The New York Times, 2025).

In addition to ambient environments, another often-overlooked issue is the indoor infiltration of wildfire smoke. People spend most of their time indoors and tend to shelter indoors during wildfire events. Research has shown that despite various mitigation strategies people apply, the mean concentration of indoor $PM_{2.5}$ can nearly triple on fire days (Liang et al., 2021; Wallace et al., 2022). Moreover, studies indicate that wildfire smoke-related VOCs can persist in indoor environments for days, even for relatively volatile compounds, providing a long-term exposure pathway for occupants (Dresser et al., 2024). Given that the wildfires in Los Angeles have lasted more than two weeks, smoke infiltration may continue for an extended period. Therefore, attention should also be paid to indoor air quality to better protect public health.
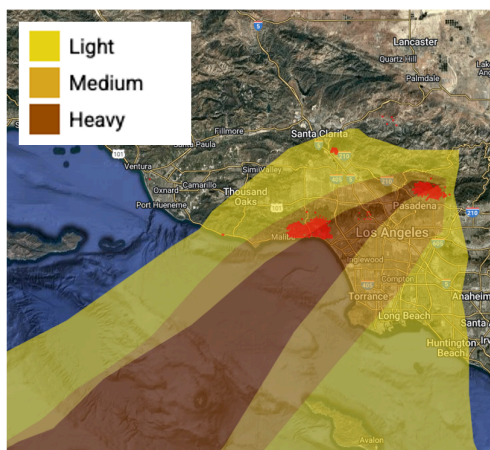
Figure 7.4. Satellite observations of smoke plume density from the NOAA Hazard Mapping System on 9 January 2025, with active fire detections in red. Note that the presence of smoke in the atmosphere does not necessarily indicate surface exposure. Data from https://globalfires.earthengine.app/view/hms-smoke.

The National Ambient Air Quality Standards (NAAQS) currently use PM2.5 as a proxy for wildfire smoke exposure. However, this approach fails to account for the specific composition of

wildfire-generated PM2.5. Additionally, it does not consider other toxic chemicals present in the smoke, especially due to the combustion of built structures.

There are many opportunities to address these challenges, for example, by revisiting air pollution monitoring during wildfires and adjusting alert thresholds when smoke is suspected. Additional research is also needed on the detailed composition of urban wildfire smoke, and the transport dynamics of smoke components. Furthermore, health authorities could develop more comprehensive monitoring systems that account for the unique characteristics of wildfire smoke.

7.5 Legislation and policy

The wildfire legislative framework in California, including Los Angeles County, operates within a multi-agency system at the federal, state, and local levels (CAL FIRE, 2024). At the state level, the California Department of Forestry and Fire Protection (CAL FIRE) leads wildfire prevention, response, and recovery efforts, guided by regulations such as the Public Resources Code §4291 and directives within the 2024 CAL FIRE Strategic Plan. Federally managed lands adjacent to Los Angeles County are under the jurisdiction of agencies like the U.S. Forest Service and the Bureau of Land Management (BLM), each enforcing specific fire mitigation policies.

Local authorities implement tailored wildfire ordinances, focusing on vegetation clearance, defensible space, and fire-resistant construction codes. Chapter 7 of the California Building Codes (CBC) outlines detailed guidance for fire prevention in construction, including fire-resistant materials and home hardening measures, and chapter 7A provides additional detail specific to the Wildland-Urban Interface (California Building Code, 2022). At the state level building codes require 100 feet of defensible space around structures in high-risk areas, however in the City of Los Angeles a more stringent 200 feet is required. (CAL FIRE, LAFD 2025)

Often following major wildfires, various legislative protections have evolved in Los Angeles. In 1971 Fire Buffer Zones were established as a result of the Chatsworth Fire. In 1981 LAFD established the Brush Clearance Unit to inspect the Mountain Fire District for compliance. In 1986, following the Baldwin Hills Fire, the Brush Clearance Inspection Program was expanded. Following the Oakland Hills Fire in 1993 Very High Fire Hazard Severity Zones were enacted. In 1997, fire defensive zones were extended to 200 feet. Following the Oakland Hills Fire and the Cedar Fire, a joining program between the Fire Department and Department of Transportation clears illegally parked vehicles on Red Flag Days in Very High Fire Hazard Severity Zones. (LAFD 2025)

In 2019 the California legislature passed AB 38 which requires fire risk disclosure to home buyers in high risk and very high risk fire zones. Example disclosures include: roof coverings that are made of untreated wood shingles, combustible landscaping within 5 feet of the home, non tempered glass windows, missing roof flashing, among others. (CA Legislature 2025) In 2021 the California legislature also passed AB 9 which established the Regional Forest and Fire Capacity Program in the Department of Conservation, created a deputy director of Community Wildfire Preparedness and Mitigation and established a Community Wildfire Mitigation Assistance Program. (CA Legislature 2025a)

In 2020 a bill was proposed to require local governments to reduce building in fire-prone areas, introduce stricter building codes, brush management and road design standards in new homes and subdivisions that are at high risk. However, the bill was vetoed by the governor due, in part, to its impact on the availability of housing in California which is another major issue in the state (CalMatters, 2025).

The State of California also has a variety of climate change laws including: a Greenhouse Gas (GHG) Emission Reduction law that requires California to reduce its GHG emissions to 40% below 1990 levels by 2030; renewable energy procurement bills that require the state to procure 60% renewable energy by 2030 and have 100% carbon-free energy by 2045. The State also has various mitigation measures associated with transportation such as gasoline taxes, vehicle emissions targets and electric vehicle infrastructure. The State also has various adaptation oriented legislation such as a Climate Adaptation Strategy, the Integrated Climate Adaptation Resiliency Program and various bills that require local governments to incorporate adaptation and resiliency into plans and strategies, requiring state agencies to factor in climate change in new infrastructure planning, and measures for risk transfer. California legislation also requires that at least 25% of the States revenue from its cap-and-trade program is directed toward projects that support disadvantaged communities (UC Berkeley).

At the federal level there are a variety of disaster laws and government social protection systems in place to aid in response and recovery of disaster affected communities. These include: FEMA's Individual and Household Assistance Program, and Disaster Legal Services Program. The US Department of Labor's Disaster Unemployment Assistance program was activated on January 14th 2025, which provides unemployment benefits for up to 26 weeks. The USDA's various Child Nutrition Programs such as the Supplemental Nutrition Assistance Program, and National School Lunch Program. The US Small Business Administrations Physical Damage Loan program and the Economic Injury Disaster Loan program (Clarke et al 2024, US DOL 2025, CA OES 2025, USDA 2025)

V&E conclusions

Los Angeles' wildfire prevention strategy emphasizes early detection, fuel reduction, and community preparedness, with tools like satellite-based fire monitoring and automated weather stations aiding rapid response. The 2025 wildfires, driven by extreme Santa Ana winds and exacerbated by drought and vegetation buildup, highlighted the need for enhanced evacuation coordination, defensible space enforcement, and mitigation measures such as ember-resistant zones and the Community Wildfire Protection Plan to address increasing wildfire risks. California's wildfire legislative framework involves a multi-agency system at the federal, state, and local levels, with California Department of Forestry and Fire Protection (CAL FIRE) leading state wildfire prevention and response efforts. While regulations such as the California Building Code and Public Resources Code §4291 aim to enhance fire resilience, challenges remain in enforcement, interagency coordination, and resource allocation, underscoring the need for stronger cooperation and community-based prevention programs. In addition, water infrastructure in LA is designed for more routine, structural fires, not the

unprecedented and continuous needs posed by a fast-moving wildfire. However, as the likelihood of extreme FWI conditions increases with climate change, wildfires are likely to increasingly impact urban and suburban areas necessitating more robust water infrastructure that is able to handle higher needs.

Data availability

All time series used in the attribution analysis are available via the Climate Explorer.

References

All references are given as hyperlinks in the text.

Appendix

A1 Model evaluation tables

Before synthesising the observation-based and climate model results, the climate models are first evaluated against the gridded observational data products for their ability to capture the seasonal and spatial patterns of daily maximum temperatures and precipitation in the study region. The models are then evaluated on how closely the parameters of the fitted statistical model (the standard deviation when using a normal distribution, and the scale and shape parameters when using a GEV) match those estimated using the observational datasets. The correlation between the variable of interest and the OND Niño3.4 index is also checked. Each parameter estimate is labelled as 'good' if the best estimate falls within the bounds estimated from the observations; 'reasonable' if the confidence interval for the model overlaps with the range estimated from the observations; or 'bad' if the ranges do not overlap. If the model is 'good' for all criteria, we give it an overall rating of 'good'. We rate the model as 'reasonable' or 'bad', if it is rated 'reasonable' or 'bad', respectively, for at least one criterion.

In Tables A1.1-A1.3 below we show the results of the model validation for FWI1X, SPI-OND and DC-DOY over the study region. All of the models were deemed to capture the seasonal pattern of temperatures, and the spatial patterns of precipitation and temperature, reasonably well, and so these results are not reported individually. Due to the small size of the study region, and the need for temperature, precipitation, humidity and wind data, only a small number of climate models were available for inclusion in the FWI1X analysis, and therefore it was necessary to retain models deemed 'reasonable' in the synthesis, as well as 'good' models. For SPI-OND, which requires only monthly precipitation data, more models were available and so only 'good' models were retained. For DC-DOY, which requires daily tasmax and precipitation for the calculation of the drought code, fewer models were again available and so both 'good' and 'reasonable' models were included. Where more than one version of the same model passed the evaluation step - for example, HadGEM3-GC31-HM and HadGEM3-GC31-MM - only the higher resolution model was retained, with one exception:

CNRM-CM6-1-HR was found to simulate an implausibly large decrease in rainfall, so the CNRM-CM6-1 variant was retained in the analysis of SPI-OND instead.

Reanalysis / models	20-year FWI1X	Scale parameter	Shape parameter	Evaluation
ERA5	29.2	5.95 (4.84, 6.97)	-0.02 (-0.18, 0.18)	
CanESM2_CanRCM4	25.9	6.26 (5.28, 7.32)	-0.56 (-0.88, -0.35)	bad
CanESM2_CRCM5-UQAM	26.5	5.78 (4.79, 7.17)	-0.45 (-0.84, -0.23)	bad
CanESM2_RCA4	18.6	4.66 (3.76, 5.62)	-0.51 (-0.84, -0.33)	bad
GFDL-ESM2M_RegCM4	26.8	5.98 (4.94, 7.02)	-0.29 (-0.58, -0.11)	reasonable
GFDL-ESM2M_WRF	27.1	6.00 (4.3, 7.54)	-0.20 (-0.55, 0.21)	reasonable
HadGEM2-ES_RegCM4	28.3	5.77 (4.55, 7.03)	-0.41 (-0.72, -0.18)	bad
HadGEM2-ES_WRF	28.3	6.56 (5.64, 7.75)	-0.64 (-0.94, -0.48)	bad
MPI-ESM-LR_CRCM5-UQAM	24.6	4.73 (3.81, 5.48)	-0.24 (-0.48, -0.07)	reasonable
MPI-ESM-LR_RegCM4	25.4	5.51 (4.54, 6.34)	-0.25 (-0.48, -0.06)	reasonable
MPI-ESM-LR_WRF	25.4	5.42 (4.4, 6.41)	-0.29 (-0.52, -0.09)	reasonable
MPI-ESM-MR_CRCM5-UQAM	25.5	5.13 (3.92, 6.03)	-0.24 (-0.44, 0.03)	reasonable

Table A1.1: *Evaluation of the climate models considered for attribution of January FWI1X over southern California (all CORDEX NAM-22). For each model, the best estimates of the scale and shape parameters of the fitted GEV are shown, along with 95% confidence intervals obtained via bootstrapping. The overall evaluation is shown in the right-hand column. All models were judged 'reasonable' in terms of spatial pattern and seasonal cycle, so the results of this step are not shown. Models excluded from the final synthesis are shaded grey.*

	Reanalysis / models	20-year SPI-OND	Scale parameter	ENSO correlation	Evaluation
	ERA5	-1.81	0.93 (0.78, 1.03)	0.2 (0, 0.4)	good
CORDEX	NAM-22_CNRM-CM5_CRCM5	-1.4	0.91 (0.76, 1.01)	0.25 (0.07, 0.45)	good
	NAM-22_GFDL-ESM2M_CRCM5	-0.84	1.03 (0.86, 1.15)	0.2 (-0.01, 0.38)	good
	NAM-22_GFDL-ESM2M_WRF	-0.95	1.1 (0.91, 1.24)	0.14 (-0.08, 0.34)	reasonable
	NAM-22_HadGEM2-ES_REMO2015	-1.5	0.83 (0.6, 1.03)	0.15 (-0.03, 0.33)	good
	NAM-22_HadGEM2-ES_WRF	-1.32	0.85 (0.72, 0.95)	0.19 (0.02, 0.36)	good
	NAM-22_MPI-ESM-LR_REMO2015	-0.95	0.8 (0.61, 0.92)	0.18 (-0.04, 0.38)	good
	NAM-22_MPI-ESM-LR_WRF	-1.4	0.99 (0.83, 1.12)	0.23 (0.04, 0.38)	good
	NAM-22_MPI-ESM-MR_CRCM5	-1.19	0.85 (0.71, 0.95)	0.13 (-0.05, 0.32)	good
	NAM-22_NorESM1-M_REMO2015	-1.04	0.88 (0.72, 0.99)	0.15 (-0.05, 0.34)	good
	NAM-44_CanESM2_CanRCM4	-1.54	1.06 (0.92, 1.17)	0.25 (0.08, 0.42)	reasonable
	NAM-44_CanESM2_CRCM5	-1.38	0.9 (0.76, 1.02)	0.25 (0.07, 0.41)	good
	NAM-44_HadGEM2-ES_WRF	-1.34	0.85 (0.72, 0.94)	0.17 (0, 0.33)	good
HighResMIP	CMCC-CM2-HR4	-1.25	0.7 (0.57, 0.79)	-0.12 (-0.31, 0.1)	lower-res duplicate
	CMCC-CM2-VHR4	-1.83	0.9 (0.78, 0.99)	-0.12 (-0.33, 0.11)	reasonable
	CNRM-CM6-1	-1.93	1.17 (0.93, 1.35)	-0.04 (-0.3, 0.24)	reasonable
	CNRM-CM6-1-HR	-2.22	1.07 (0.87, 1.22)	-0.11 (-0.28, 0.09)	Implausible
	EC-Earth3P	-1.58	0.93 (0.74, 1.08)	-0.07 (-0.3, 0.15)	reasonable
	HadGEM3-GC31-HM	-1.65	1.03 (0.86, 1.15)	-0.23 (-0.43, -0.02)	bad
	HadGEM3-GC31-LM	-1.75	1.01 (0.82, 1.13)	-0.12 (-0.35, 0.13)	lower-res duplicate
	HadGEM3-GC31-MM	-1.36	0.91 (0.76, 1.02)	-0.01 (-0.19, 0.19)	reasonable
	MPI-ESM1-2-HR	-1.58	0.92 (0.76, 1.03)	-0.24 (-0.46, 0.01)	lower-res duplicate
	MPI-ESM1-2-XR	-1.98	1.11 (0.93, 1.25)	0.2 (-0.02, 0.41)	reasonable
	MRI-AGCM3-2-H	-1.99	0.94 (0.76, 1.06)	0 (-0.26, 0.23)	reasonable
	MRI-AGCM3-2-S	-2.66	1.39 (1.09, 1.61)	0.01 (-0.25, 0.21)	bad
IPSL ensemble	IPSL-CM6A-ATM-HR	-1.53	0.96 (0.78, 1.08)	0.12 (-0.11, 0.38)	good
	IPSL-CM6A-ATM-ICO-HR	-1.83	1.13 (0.93, 1.26)	0.07 (-0.17, 0.3)	reasonable
	IPSL-CM6A-ATM-ICO-LR	-1.76	0.95 (0.77, 1.09)	-0.09 (-0.29, 0.11)	reasonable
	IPSL-CM6A-ATM-ICO-MR	-2.27	0.91 (0.72, 1.04)	0.01 (-0.19, 0.23)	good
	IPSL-CM6A-ATM-ICO-VHR	-2.21	0.95 (0.75, 1.09)	0.03 (-0.22, 0.3)	good
	IPSL-CM6A-LR	-1.89	1.08 (0.87, 1.21)	0.13 (-0.1, 0.35)	reasonable
	IPSL-CM7A-ATM-HR	-2.15	0.94 (0.78, 1.05)	0.09 (-0.15, 0.31)	good
	IPSL-CM7A-ATM-LR	-1.71	0.91 (0.72, 1.04)	0.13 (-0.1, 0.36)	good

Table A1.2: *Evaluation of the climate models considered for attribution of SPI-OND over southern California. For each model, the best estimate of the scale parameter of the fitted normal distribution and correlation between OND Niño3.4 and SPI-OND are shown, along with 95% confidence intervals obtained via bootstrapping. The overall evaluation is shown in the right-hand column. All models were judged 'reasonable' in terms of spatial pattern and seasonal cycle, so the results of this step are not shown. Models excluded from the final synthesis are shaded grey.*

	Reanalysis / models	10-year DC-DOY	Scale parameter	ENSO correlation	Evaluation
	ERA5		34.36 (28.44, 39.3)	-0.19 (-0.4, 0.03)	
CORDEX	NAM-22_GFDL-ESM2M_CRCM5	113	44.04 (37.46, 49)	0.17 (0.0, 0.34)	reasonable
	NAM-44_CanESM2_CanRCM4	174	30.63 (26.04, 33.5)	-0.09 (-0.27, 0.08)	good
	NAM-44_CanESM2_CRCM5	177	29.64 (25.18, 32.72)	-0.03 (-0.19, 0.14)	good
	NAM-44_GFDL-ESM2M_RegCM4	91	35.68 (27.98, 41.26)	-0.08 (-0.27, 0.12)	good
	NAM-44_HadGEM2-ES_RegCM4	89	37.72 (25.56, 51.06)	-0.13 (-0.28, 0.02)	good
	NAM-44_MPI-ESM-LR_CRCM5	142	49.38 (40.06, 55.97)	0.08 (-0.11, 0.25)	bad
	NAM-44_MPI-ESM-LR_RegCM4	109	35.78 (28.43, 41.97)	-0.1 (-0.27, 0.06)	good
	NAM-44_MPI-ESM-MR_CRCM5	128	39.45 (31.12, 45.64)	-0.15 (-0.32, 0.03)	reasonable
HighResMIP	CNRM-CM6-1	108	32.76 (25.43, 38.18)	-0.01 (-0.27, 0.25)	good
	EC-Earth3P	147	28.15 (22.4, 32.49)	-0.04 (-0.29, 0.21)	reasonable
	HadGEM3-GC31-HM	170	37.74 (30.94, 41.91)	0.11 (-0.1, 0.31)	reasonable
	HadGEM3-GC31-LM	148	35.06 (28.42, 39.97)	0.0 (-0.25, 0.27)	duplicate
	HadGEM3-GC31-MM	143	33.82 (26.69, 39.03)	0.0 (-0.22, 0.22)	duplicate
	MPI-ESM1-2-HR	136	25.58 (20.37, 29.4)	0.27 (0.03, 0.47)	bad
	MPI-ESM1-2-XR	152	30.96 (25.55, 34.97)	-0.05 (-0.24, 0.17)	good

Table A1.3: Evaluation of the climate models considered for attribution of DC-DOY over southern California. For each model, the best estimate of the scale parameter of the fitted normal distribution and correlation between OND Niño3.4 and DC-DOY are shown, along with 95% confidence intervals obtained via bootstrapping. The overall evaluation is shown in the right-hand column. All models were judged 'reasonable' in terms of spatial pattern and seasonal cycle, so the results of this step are not shown. Models excluded from the final synthesis are shaded grey.

A2 Multi-method multi-model attribution

Tables A2.1-A2.3 show probability ratios (PR) and changes in intensity in FWI1X, SPI-OND and DC-DOY over the study region, for ERA5 and for those models that passed the evaluation described in Section A1. These changes are synthesised into a single overarching attribution result for each index in Sections 3.1.2, 3.2.2 and 3.3.2.

A3 Normalized Mean Error of the ISIMIP Models

Table A3.1: Normalized Mean Error scores for each of the models in the three regions. Note that CLASSIC has an error score of NaN in Southern California because calculating relative anomalies was impossible. We calculated the annual NME scores and the ranked monthly NME scores.

		Observation	FireCCI5.1		GFED5	
		NME	NME3_ranked	NME3_annual	NME3_ranked	NME3_annual
Region	Model					
Southern California	CLASSIC		NaN	NaN	NaN	NaN
	JULES		1.317621	1.439291	1.308779	1.405082
	LPJ-GUESS-SIMFIRE-BLAZE		1.048789	1.225605	1.067245	1.299782
	LPJ-GUESS-SPITFIRE		1.268887	1.286112	1.283732	1.229525
	ORCHIDEE-MICT-SPITFIRE		1.21926	1.34575	1.215555	1.369222
	SSiB4		1.219743	1.435942	1.216417	1.457205
	VISIT		1.226004	1.102678	1.259634	1.17046
Ecoregion	CLASSIC		0.793876	1.206854	1.040367	1.260335
	JULES		0.963494	1.217306	1.173051	1.280394
	LPJ-GUESS-SIMFIRE-BLAZE		0.906061	1.421871	1.09876	1.585881
	LPJ-GUESS-SPITFIRE		1.076278	1.307555	1.193333	1.262123
	ORCHIDEE-MICT-SPITFIRE		1.283899	1.638516	1.336998	1.796147
	SSiB4		0.856338	1.143692	1.013346	1.259695
	VISIT		1.142135	1.216597	1.21184	1.351223

California	CLASSIC	0.664232	0.883692	0.944722	1.090641
	JULES	0.878965	0.841268	1.048078	0.865311
	LPJ-GUESS-SIMFIRE-BLAZE	0.813226	1.229929	1.017667	1.368196
	LPJ-GUESS-SPITFIRE	0.957316	1.332816	1.037009	1.356217
	ORCHIDEE-MICT-SPITFIRE	1.214527	1.287428	1.281636	1.433707
	SSiB4	0.71142	0.972715	0.914142	1.058775
	VISIT	1.125734	1.190924	1.235055	1.337232